School of Chemistry

A Study of the Breakdown and Discharge Behaviour of Microhollow Cathode Discharge Devices and the Effect of the Cathode Material and Morphology

Max Williams

April 2016

This thesis is submitted in partial fulfilment of the requirements for the Honours Degree of MSci (Bsc) at the University of Bristol

Supervisor: Prof. Paul May
Second Assessor: Dr. Neil Fox
Bristol Diamond Group

Abstract

A series of microhollow cathode discharge devices were fabricated, using either commercially grown boron-doped diamond (BDD) or extrinsic silicon wafers as the cathode and a CVD insulating intrinsic diamond dielectric. Devices with a range dielectric thicknesses and cathode hollow diameters of 150 µm or 300 µm, the breakdown voltage scaling and I-V characteristics were investigated in He and Ar at pressures ranging 50 - 3000 Torr cm.

Breakdown voltages of BDD, p-type silicon and n-type silicon cathode devices were found to be similar across the range pressures tested, with two different behaviours in response to changing pressure reproducibly measured, most likely due to morphology changes of the cathode hollow. While BDD cathodes were subject to conversion of diamond-like carbon to graphite under the sputtering action of He and Ar ions during operation. Silicon was thought to form insulating nitride and oxide species in addition to re-deposited silicon on the cathode hollow surface due to heating and sputtering effects.

The breakdown curves for four microhollow cathode devices were fitted to a modified Paschen's law and values for the gas constants A, B and γ were found empirically using a simultaneous least squares minimisation fit for pairs of breakdown curves. It was found that changes to the hollow morphology reduced electron mean free paths, likely resulting from reduced probabilities of long path breakdown. However, due to strong correlation between the gas constants, a change in γ following morphology changes could not be concluded.

I-V curves of the devices in both He and Ar were recorded, verifying the operation of the devices in the normal glow, in agreement with literature. At lower pressures the plasma was observed to spread to the copper lid of the device holder, preventing the discharge from entering the abnormal glow regime, with the abnormal glow only seen at high pressures.

Contents

1. Introduction

1.1. Introduction to Plasma

Plasma, the forth state of matter is thought to make up as much as 95% of matter in the universe.[74] While it occurs in abundance elsewhere in the universe, below the Earth's atmosphere[72] plasma is only produced naturally by lightning and the aurora.[74]

Plasma is a state of matter containing significant amounts of free charged particles, dominating the state's properties through the action of electromagnetic forces.[72] The presence of even a small fraction of charged particles in a plasma allow it to become a strong conductor of electricity depending it its degree of ionization. At 0.1% ionization a plasma is 50% of its maximum conductivity and metal-like conductivity is reached at just 1% ionization.[88]

Plasma environments, rich in high energy electrons, ions and excited neutral gas atomsm can provide extremely reactive conditions making plasma a powerful tool in industrial etching, sputtering and deposition processes.[13] With the development of high non-equilibrium plasmas, with gas temperatures close to room temperature, plasmas have become useful in many environmental and medical applications such as pollutant decomposition and sterilisation.[19,27,39]

1.2. Plasma Production

To create a plasma, atoms must have an electron removed from their outer shells, forming a positively charged ion and a free electron. There are multiple ways to ionize a gas to form a plasma, heating a gas to energies similar to the binding energy of its lowest energy electrons or invoke the use of radiation or lasers to split an atoms from its outer electrons.[17] The most efficient way of producing a plasma is the use of high voltages to accelerate electrons into gas molecules, ionizing them in a 'gas discharge'.

The creation of plasma via the use of electric fields occurs naturally in the form of lightning, with man-made gas discharge lamps having existed before even the electron was discovered.[9] Gas discharges, or the "flow of electric current through a gaseous medium",[34] allow charge to flow between electrodes separated by a gas, provided ionizing electrons can undergo various processes to sustain a sufficient degree of ionization. If sufficient current can be supplied, a plasma can form between the electrodes of a gas discharge device.[17]

1.3. Types of Gas Discharge

A gas discharge can be characterised by the amount of current carried by the gas, and are thus divided into three different types: the Townsend discharge, the glow discharge and the arc discharge. On a current-voltage (I-V) plot, all three types can be identified by the characteristic relationship of the voltage drop and current flow between the electrodes.[34] A general I-V plot of a gas discharge is shown in figure 1.1.

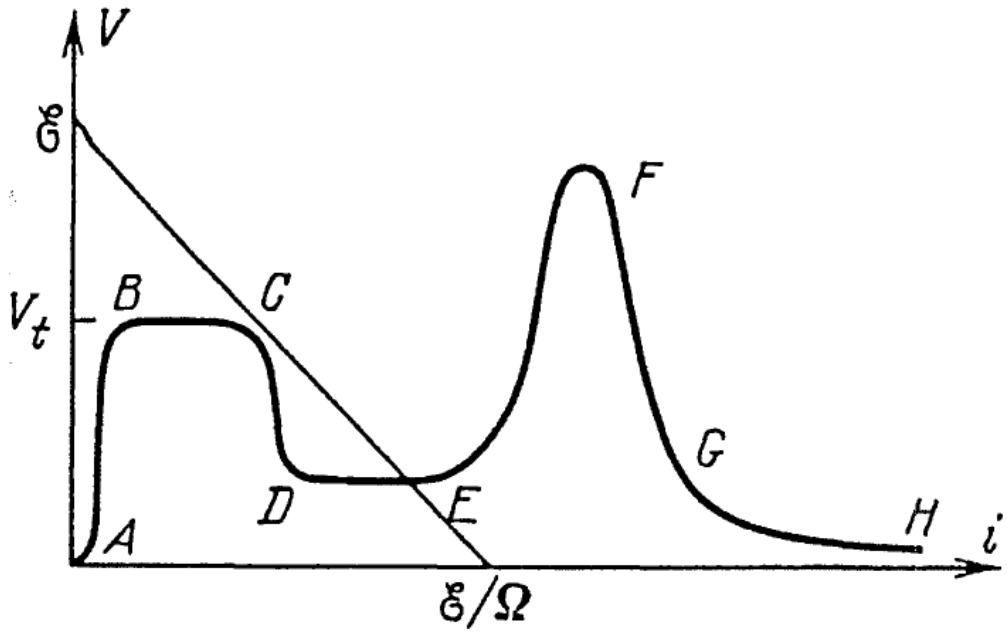

Figure 1.1: Current-Voltage plot of a gas discharge, reproduced from *Gas discharge physics* (1991).[73]

1.3.1. Townsend Discharges

As the voltage across the electrodes is increased from zero, an almost immeasureably small current will be flowing, due to the acceleration of small numbers of free electrons and ions produced by cosmic rays.[66] As the voltage is further increased, the current due these externally produced ions and electrons soon saturates as all the externally produced particles are now able to reach their respective electrode (figure 1.1, label A).

At a voltage known as the breakdown voltage (V_b), a discharge becomes self-sustaining and the creation of free electrons by cosmic rays is no longer required.[34] A plasma becomes self-sustaining at the breakdown voltage due to an electron avalanche, where electrons initially produced between the electrodes by incident cosmic rays are accelerated with sufficient energy towards the anode. These accelerated electrons are able to ionize gas atoms on the way to the anode to form ions and additional free electrons, which are in turn able to be accelerated by the field. Ions produced are accelerated towards the cathode, sometimes causing the emission of a secondary electron on collision with the cathode. While electron avalanches can occur below the breakdown voltage, only above V_b are sufficient ions produced to generate at least one additional electron to start a new electron avalanche.

Although the discharge is self-sustaining, the ionization and excitation of neutral gas atoms is still very low, meaning that little radiation is emitted. At label B on figure 1.1 the breakdown voltage has been reached and the discharge is now current limited rather than voltage limited below the breakdown voltage. The 'Townsend Dark Discharge' region of the I-V curve that exists for current values ranging $\sim 10^{-10} - 10^{-5}$ A, or between labels A and C on figure 1.1.[73]

1.3.2. Glow Discharges

At currents between $\sim 10^{-6} - 10^{-1}$ A, the discharge can transition to the glow discharge regime, sustained at a voltage much lower than the initial breakdown voltage. This transition can be seen between labels C and D on figure 1.1. The glow discharge is normally split into a relatively flat region on an I-V curve, where current and voltage become independent of each other and a region of rising voltage with increasing current, known as the normal glow and abnormal glow respectively. These regions are bounded by labels D and F on figure 1.1, with the abnormal glow existing from E to the transition to the arc discharge at label F.

1.3.3. Arc Discharges

When current flow is allowed to approach 1 A, the transition-to-arc from the abnormal glow occurs. An arc discharge is characterised by a very low sustaining voltage, ordinarily an order of magnitude less than that of the normal glow discharge. When the arc discharge regime is reached, electron emission due to cathode ion bombardment is considerably less efficient due to the reduced voltage drop across the electrodes.[34] Two alternate electron emission mechanisms take over from the now less efficient ion bombardment mechanism, thermionic and field emission from the cathode. The cathode is strongly heated by increasing ion bombardment even before the glow-to-arc transition in the abnormal glow, to the point where thermionic emission of electrons from the cathode becomes significant.[53,73] In higher pressures arcs, the cathode sheath also becomes incredibly thin (fractions of a millimetre) resulting in strong electric fields close to the surfaceof the cathode, causing the tunnelling of electrons from the cathode surface to the vacuum, known as field emission.

1.3.4. Regions of the Glow Discharge

When a gas discharge is operating as a glow discharge, the space between the electrodes is made up of a number of regions with different luminosities, particle number densities and electric fields. These regions which exist within a glow discharge are shown in figure 1.2 for a parallel-plate electrode discharge, one of the most simple gas discharge geometries.

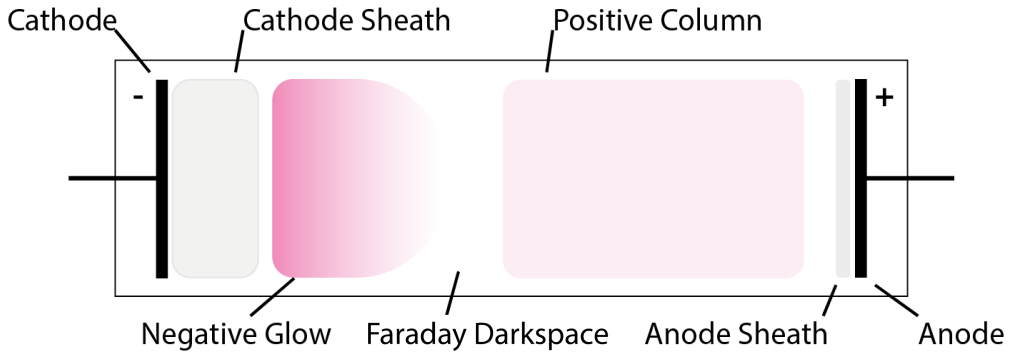

Figure 1.2: Diagram of the regions present in a glow discharge. The relative size of the regions are not to scale. Adapted from *Fundamentals of gaseous ionization and plasma electronics* (1971).[60]

Adjacent to the cathode is a region called the cathode sheath (or cathode fall) which due to a build up of positive space charge near to the cathode, contains almost all of the voltage drop between the two electrodes.[66] A glow discharge cannot exist without the cathode sheath as it is responsible for the acceleration of electrons produced through the ion bombardment of the cathode. Some secondary electrons produced at the cathode are able to pass through the sheath without collision and thus have an energy equal to the potential drop across the cathode sheath. Elastic and inelastic scattering of electrons with neutral gas atoms within the cathode sheath create a distribution of electron electrons leaving the cathode sheath, up to the voltage drop across the cathode sheath.[9,13]

Next to the relatively dark cathode sheath is the negative glow, the most luminous part of the discharge. It is formed due to high energy electrons accelerated from the sheath to form a self-sustaining electron avalanche, causing the emission of radiation due to relaxation processes within the exited gas atoms. Closer to the anode, the luminosity of the negative decreases, caused by a reduction in the rate of excitation and relaxation as electrons are slowed down following inelastic collisions with gas molecules.[9]

Moving towards the anode out of the negative glow and through a region called the Faraday dark space, a second luminous region called the positive column exists.[73] The positive column in a region of are equal numbers of both positive and negative particles, although the ionization fraction is still low, between 10^{-5} and 10^{-6}.

Finally before reaching the anode, there is a second sheath region called the anode sheath (or anode fall). The voltage drop in the anode shealth is much smaller than the cathode sheath and being much thinner than the cathode fall often makes it difficult to observe.[9,13]

If the two electrodes are brought closer together, the positive column and Faraday dark space are consumed leaving, the electrode fall regions and negative glow. Specific inter-electrode distances are often used remove the positive column for use in many industrial glow discharge processes. Once the electrode separation is reduced to below approximately twice the cathode sheath thickness the cathode sheath becomes distorted in shape and the discharge disappears.[13]

1.3.5. Abnormal Glows

The structure of the normal and abnormal glow discharge are identical, with the coverage of the cathode by negative glow determining whether the discharge is in the abnormal or normal glow. Throughout the normal glow region of the I-V curve, the current density within the negative glow is constant because as the current is increased, the negative glow expands to cover more and more area of the cathode (figure 1.3). Once the negative glow completely coveres the cathode, it can no longer expand and the current density must increase, requiring more voltage to do so, entering the abnormal glow at E on figure 1.1.[13]

1.4. Microdischarges

Microdischarges are gas discharges where at least one dimension of the electrode geometry is less than 1 mm,[21] changing many of the operating characteristics of the resulting discharge.

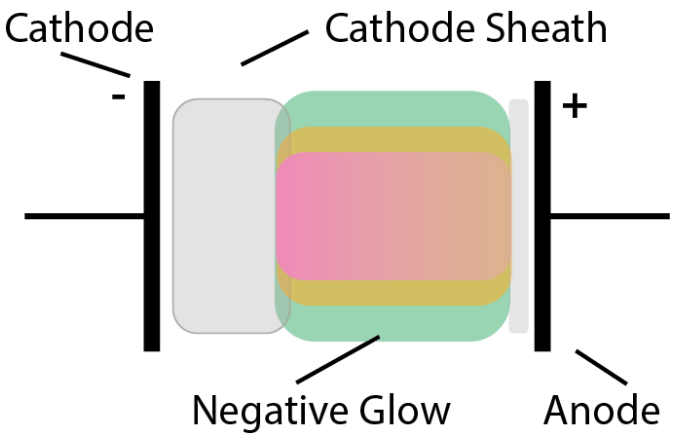

Figure 1.3: Diagram showing expansion of the negative glow from the normal glow (pink, yellow) to the abnormal glow (green), when the cathode is completely covered by the negative glow. The relative sizes of the regions are not to scale.

Microdischarges have been shown to be extremely useful in the generation of stable plasma at high pressures, approaching or even exceeding atmospheric pressure. Microdischarges have displayed increased electron and current densities as well an improved ability to create extremely non-equilibrium plasmas compared to conventional macroscopic discharge apparatus.[7,51] Microdischarges operating in the glow discharge regime can be generated using a plethora of different device designs, constructed from a large range of materials by a range of fabrication techniques and driven by DC to RF power sources. This thesis will be concentrating on DC driven discharges operating in the glow discharge regime.

1.4.1. Paschen's Law

In 1889, Friedrick Paschen investigated the breakdown behaviour of parallel plates using various gases, gas pressures and electrode separations.[65,67] From these investigations he showed empirically, that the breakdown voltage scaled logarithmically with the product of pressure and electrode separation only (pd). He formulated an equation describing the behaviour of the breakdown voltage of a gas with the value of pd, depending on the gas and more weakly on the electrode material. Paschen's equation is shown in equation 1:

$$V_b = \frac{Bpd}{\ln(Apd) - \ln\left(\ln\left[1 + \frac{1}{\gamma_{se}}\right]\right)} \tag{1}$$

where A and B are the saturation ionization constant and the inelastic electron-molecule collision barrier of the gas respectively while γ is the Townsend secondary ionization coefficient of the cathode by ion impact of the gas, making it also dependent on the electrode material.[31,67]

A represents the limit of $\frac{\alpha}{p}$ for a particular reduced electric field ($\frac{E}{p}$), where α is the number of secondary electrons produced per unit length by a primary electron accelerated towards the

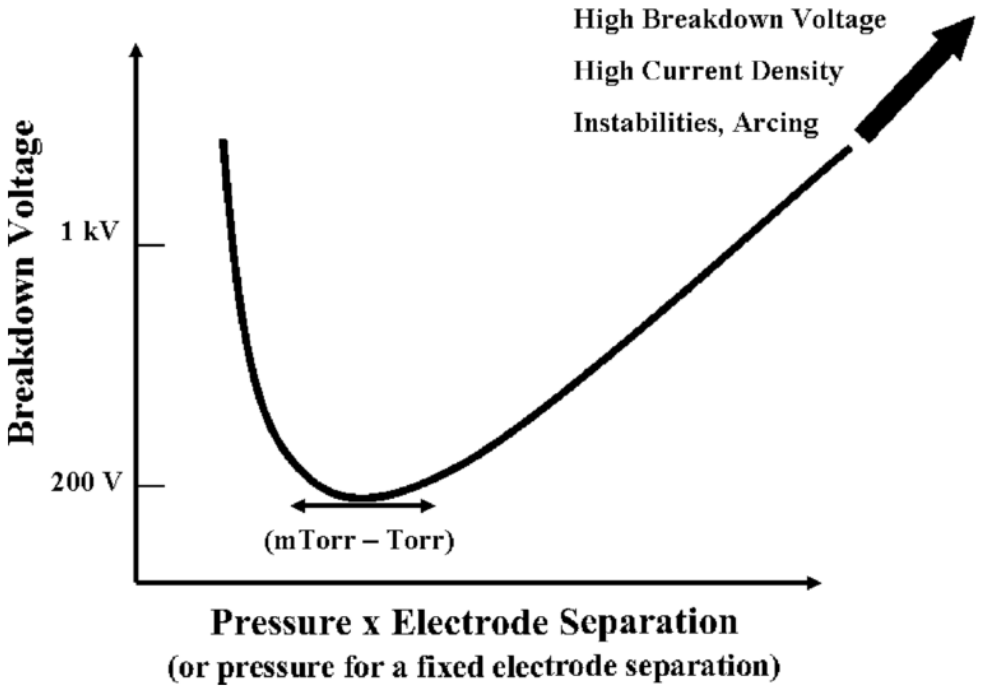

Figure 1.4: Typical behaviour of the breakdown voltage of a gas with *pd* for a parallel-plate electrode geometry. Reproduced from Foest *et al.* 2006.[21]

anode,[93] and p is the pressure. Physically, a higher value of A indicates a higher number of ionizing collisions per unit distance and therefore the mean free path of electrons is reduced.

The gas constant B is often refered to as an "effective ionization potential" which takes into account the collision cross section of the atoms involved and any losses in the rate ionization due to excitation and other processes.[93] Helium, while having an ionization potential is considerably higher than Ar (24.6 eV versus 15.8 eV),[30] has a considerably lower effective ionization coefficient (B) ($2.8\,\mathrm{Torr}^{-1}\,\mathrm{cm}^{-1}$ versus $10.2\,\mathrm{Torr}^{-1}\,\mathrm{cm}^{-1}$).[16] This discrepancy is due to differences in collision cross-section between relatively expansive argon atoms and helium atoms with tightly bound electronic structure. A higher value of B also indicates a shortened electron mean free path due to increased inelastic collisions with higher collision-cross section atoms.

γ is the second Townsend coefficient, representing the number of electrons produced via secondary electron emission on average, for a single ion of the gas.[33] As a result, the calculated value of γ for the gas is also dependent on the electrode material. Historically sodium glass electrodes have been used for empirical determination of the gas constants.[16]

The existence of a minimum breakdown voltage can be explained though the scaling of the mean free path with gas pressure. The mean free path is the distance between collisions of an electron travelling from the cathode to the anode, for an electron to start an electron avalanche it must reach ionizing energies before it collides with gas atoms. At high *pd*, the mean free path is small due to frequent collisions with gas atoms, requiring the accelerating voltage be higher to accelerate an electron to ionizing energies in a shorter distance than that at the minimum. Conversely, at very low *pd* to the left of the minimum, the gas density is so low that while the mean free path

is higher, a higher voltage is required to ensure that a sufficient proportion of electrons have the energy required to ionize enough gas atoms, sustaining an electron avalanche.[3,34]

However for conventional, macroscopic glow discharges, moving towards atmospheric pressures pushes the breakdown voltage to much higher values due to Paschen's law, increasing the tendency for discharges to transition to an arc and increasing current densities. In macroscopic geometries the minimum occurs between 1 - 10 Torr cm, corresponding to pressures on the order of mTorr. In order to operate close to the minimum breakdown voltage at much higher pressures, it should be expected that the electrode separation must be reduced to sub-millimetre dimensions and into the realm of microdischarges.[21]

1.5. Characteristics of High Pressure Microdischarges

Operation of glow discharges at close to atmospheric pressures moves the behaviour of the plasma away from the well studied single-collision dynamics of low pressure plasmas and into a highly collisional environment favouring 3-body collisional dynamics.[79]

1.5.1. Excimer Production

Excimers, or excited dimers, are short lived highly excited species which often emit in the vacuum ultraviolet (VUV) region of the electromagnetic spectrum, due to transitions from the lowest-lying $^3\Sigma_u$ state to the ground state in the case of rare gases. The formation of an Xe excimer ($Xe_2{}^*$) through electron impact ionization is shown in equations 2a - 2d.

$$e^- + Xe \longrightarrow Xe^+ + 2\,e^- \tag{2a}$$

$$Xe^+ + 2\,Xe \longrightarrow Xe_2{}^+ + Xe \tag{2b}$$

$$Xe_2{}^+ + e^- \longrightarrow Xe^* + Xe \tag{2c}$$

$$Xe^* + 2\,Xe \longrightarrow Xe_2{}^* + Xe \tag{2d}$$

These short lived species can only form through 3-body reactions shown in equations 2a - 2d, involving two ground-state atoms and an excited metastable gas atom.[43,82] Figure 1.5 shows an increase in emission intensity of VUV for a Xe microdischarge as the operating gas pressure is increased.

Excimer emission of microdischarge devices has been studied using a range of different operating gases,[6,18,43–45,59,70,79,81] with the energy required to form a metastable rare gas atom via electron impact on the order 20 to 30 eV.[43] $Ne_2{}^*$ and $He_2{}^*$ excimer emissions from microhollow cathode devices detected by Kurunczi *et al.* in 1999 and 2001 suggest significant populations of electrons with energies in excess of 17 eV and 21 eV respectively, explaining the formation of such excimer species.[43,45]

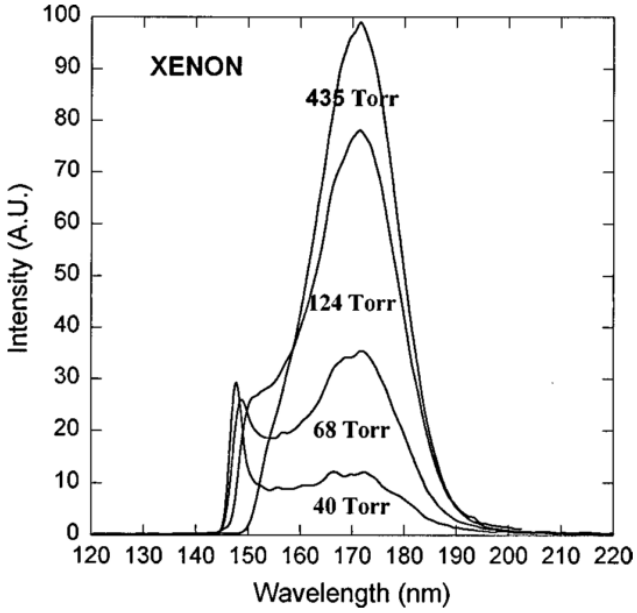

Figure 1.5: Increasing the pressure of Xe for a microhollow cathode device results in a huge increase in the emission intensity of high energy VUV excimer radiation. Reproduced from El-Habachi *et al.* 1998.[18]

1.5.2. Electron Density and Energies

There have been many attempts to measure the average energy and density of electrons present in plasma generated in microdischarge devices. Belostotskiy *et al.* measured the electron density of an argon DC parallel-plate electrode microdischarge using laser Thomson scattering, finding it to be $6 \times 10^{13}\,\mathrm{cm}^{-3}$ (50 mA),[8] much lower than values of $10^{15}\,\mathrm{cm}^{-3}$ for an Ar DC microhollow device operated at just 4 mA.[58,95]

Pulsed operation of DC microdischarges was found to substantially increase both electron densities as well as the average electron energies. Moselhy *et al.* found an increase in average electron energy from 1 eV to 2.25 eV by moving from continuous operation to 10 ns pulses.[58] The proceeding increase in the distribution of electron energy following a pulse has been found to temporarily increase rate of ionization of gas atoms, leading to an increase in electron density. The use of short ns pulses in the place of dc operation has been investigated by Stark *et al.*.[86] It has been shown in both experimental and computational studies that plasma generated using 10 ns pulsed operation could achieve comparable electron densities to dc discharges, while reducing power requirements by a factor of 150. An increase in electron temperature and densities occurs provided the pulse length was shorter than the time scale for the trasition from a glow to an arc which is around 10 ns at atmospheric pressures.[86] However, while the lower limit of pulse duration is determined by the current pulsing technology, the additional equipment costs for producing substantially shorter pulses are significant enough to potentially offset any additional savings.[86]

Average electron temperatures have been measured to be around 1 eV for both MHC[95] and parallel-plate[8] devices in Ar. However, in agreement with simulation and experimental work there has been evidence of strongly non-Maxwellian energy distributions with significant populations of electrons

with energies above 10 eV.[5,25] Kim *et al.* simulated Ar MHCDs using a 2D particle-in-cell Monte Carlo, finding that while the majority of the electrons have energies below 5 - 10 eV with a temperature of 1 eV, there exist significant populations of electrons with a temperature of 30 - 170 eV. These electrons were attributed to be pendular electrons accelerated by the cathode sheath several times before reaching the anode. A plot of the electron energy probability functions for a range of currents as a function of energy is shown in figure 1.6, where a large population of electrons with energies above 150 eV can be seen.

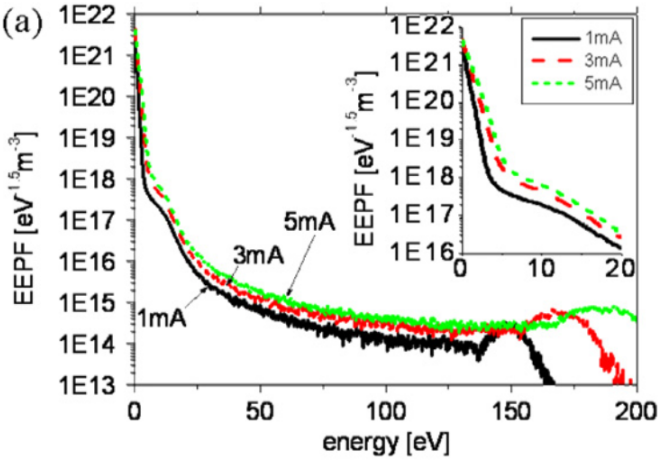

Figure 1.6: Plot showing the electron energy distribution inside a MHCD operated in 10 Torr Ar. Reproduced from Kim *et al.* 2006.[38]

1.6. Microdischarge Device Geometries

Like Paschen, many early gas discharge studies used a parallel-plate configuration of the electrodes, however using different electrode geometries can allow discharges to have substantially different characteristics, from I-V behaviour to higher current density stability.[96]

1.6.1. Microhollow Cathode

In the early 1900s, a new geometry using a hollow containing cathode became popular for many applications, especially for use in electron beam emission due to its higher cathode area and lengthened operating lifetimes.[3]

Only in the mid 1990s was the hollow cathode geometry applied to microdischarges, with the name "microhollow cathode discharges" or MHCDs coined by Karl Schoenbach.[83] Hollow cathode devices can support higher current densities over a lower forward voltage drop than conventional parallel-plate discharges[96] without undergoing the glow-to-arc transition. As a result any erosion effects resulting from device operation are reduced compared to similar arc-discharge devices.[61] A schematic of a hollow cathode microdischarge device is shown in figure 1.7.

The increased current densities generated at discharge voltages similar to parallel-plate electrode

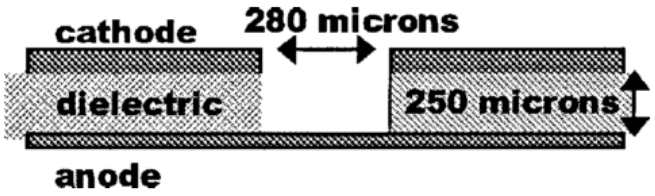

Figure 1.7: Schematic of a microhollow cathode discharge device, based on a design pioneered by Schoenbach *et al.* in 1995. Reproduced from Boeuf *et al.* 2005.[10]

geometries is primarily attributed to pendular electron motion, known as the hollow cathode effect. This pendular motion describes the oscillatory motion of the electrons caused by the bending of the electric fields coaxially into the cathode hole,[89] increasing the electron path length and the number of ionization events possible inside the device.[7,77,83] However there exists a scaling law similar to Paschen's law known as the Allis-White similarity law, relating the sustaining voltage of a discharge to *pd* and the ratio of the current flow in the discharge and the cavity diameter ($\frac{I}{D}$). By limiting the pendular electron motion to situations where the diameter of the hollow cannot exceed the lengths of two cathode falls and the negative low, a limit of pD where the hollow cathode effect can operate in reached[7], found by Schoenbach *et al.* to be roughly $pD = 1\,\mathrm{Torr\,cm}$, confirmed both computationally and experimentally.[7,23,46,63,80]

Computer models comparing computational and experimental results have also been applied to MHCD geometries. Boeuf *et al.* in 2005, used a simple model based on solutions of the fluid equations for electron and ion transport, parametrized for the hollow cathode metal-dielectric-metal device design used by Schoenbach *et al.* in 1999 (figure 1.7). It was found that with increasing current, the plasma which was once confined to the microhollow in the abnormal glow mode transitioned back into a normal mode, allowing the discharge to spread across the surface of the cathode.

Figure 1.8 shows the radiation emission of the discharge with respect to the distance from the radial distance from the cavity centre, with the vertical dotted lines representing the exent of the cavity. It can be seen that at low currents the plasma is confined to a ringed structure within the hollow before spreading 100s of microns onto the cathode surface at large current flow. It was predicted that the stability of microdischarges sustaining such high current density discharges could due to this spreading of the discharge across the cathode surface, preventing further increases to power deposition inside the hollow.[10]

In 2005, Kushner *et al.* simulated similar metal-dielectric-metal hollow devices, using a plasma-transport model including gas dynamics and operating them continuously in argon. It was theorised that because like their macroscopic counterparts, microdischarges are sustained by secondary electron emission from the cathode such that microdischarges would be susceptible to aging due to fluctuations in the secondary electron coefficient of the cathode. It was also noted that gas heating and flow dynamics become extremely important in device design due to the high current densities supported, especially in regard to excimer formation, which depend strongly on gas temperatures and rarefaction.[47]

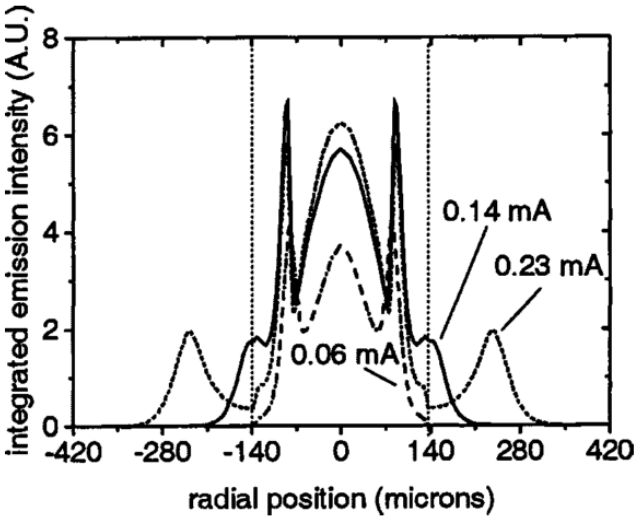

Figure 1.8: Simulated plot of the emission intensity against radial distance from the centre of the hollow cathode, with the dotted line representing the extent of the cavity. Reproduced from Boeuf *et al.* 2005.[10]

1.6.2. Other Microhollow Geometries

Many device designs are based on the cylindrical, hollow cathode (MHC) geometries, leading to designs where the hollow cathode can also act as a gas inlet for deposition applications,[75] where the anode is inserted through the walls of the hollow cathode,[2] using a screen electrode rather than an annular one,[64] and the use of critically sized slits (microslits), some of which are shown in figure 1.9.[97]

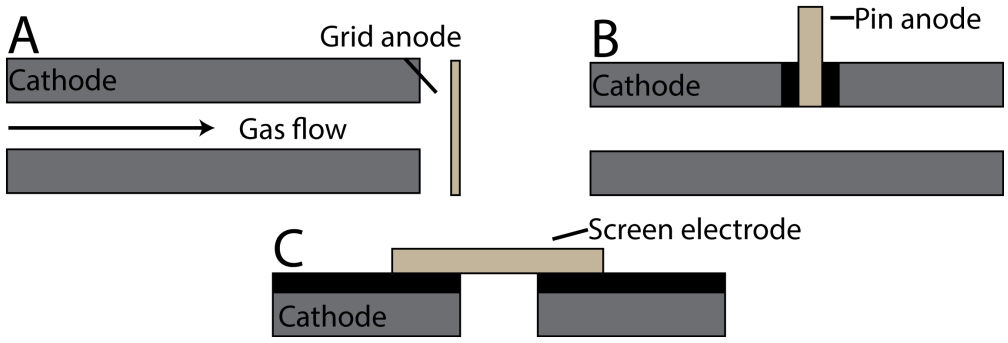

Figure 1.9: Some other geometries based on the hollow cathode geometry. **A:** Plasma jet using a grid anode and hollow cathode for deposition applications.[75] **B:** Pin anode inserted into a hollow cathode wall for modelling to assess application as a VUV radiation source. **C:** The replacement of the annular anode with a screen electrode showed a decrease in operating voltage while increasing electron temperature.[64]

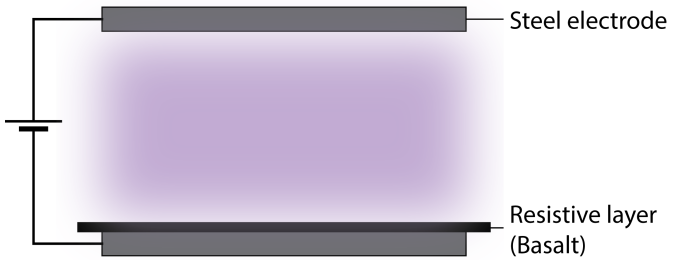

Figure 1.10: Schematic of a Resistive Boundary Discharge device, which can be operated in a glow discharge mode using AC or DC.[49,87]

1.6.3. Dielectric Barrier Discharges (DBD

Dielectric Barrier Discharges (DBD) are RF driven devices whichoften use parallel-plate electrodes covered by a dielectric layer. At atmospheric pressures the resulting discharge consists of many extremely short lived microdischarges, with their numbers dependent on the charge transferred between the plates.[24]

Work by Laroussi *et al.*[49] in 2002 aimed to create a Resistive Barrier Discharge (RBD) geometry by replacing the dielectric layer which covers one of the electrodes with a resistive layer. The inclusion of the resistive barrier allowed DC operation at atmospheric pressures without the requirement for expensive RF power supplies that can produce EM fields which can interfere with nearby sensitive electronics.[49] RBDs allow the creation of a large number of glow discharges, like DBDs, without arcing and the subsequent breakdown of the uniformity of the plasma, making them useful in many sterilization applications.[87] However, the behaviour of the plasma still requires addtitional research into its stabilisation and energy distribution as much of the energy presently heats the resistive layer rather than the plasma itself.[87]

1.6.4. Microhollow Sustained Discharges (MHSD)

There is also an electrode design built off the common MHCD design, with the addition of a second anode situated some distance from the anode of the MHCD system, as shown in figure 1.11. The use of Microhollow Cathode Discharges or MHSDs have been shown to be an effective method of generating high volumes of plasma at high pressures, while still keeping the discharge system as simple as possible.[62] When the MHCD is operated as a glow discharge, a bias of only $100\,\mathrm{V\,cm^{-1}}$ is required for electron to be directed towards the second anode to become an electron source for a larger volume plasma to grow. Figures 1.11 and 1.12 show a schematic and photograph of a MHCD forming a MCSD. Importantly, the MCSD system can be applied to any gas to obtain high pressure, high volume discharges, allowing great potential in its application to surface treatments such as thin-film deposition and metal surface modification,[85] as well as pollutant detoxifcation.[62]

MCSDs have also been modelled, with Makasheva *et al.* in 2007 using the similarities between plasma in MHCD and the plasma that exists between the MHCD and the second anode to model the high pressure plasma in MHCDs without complications introduced during modelling of the cathode regions. They were able to demonstrate the validity of a self-consistent quasi-neutral

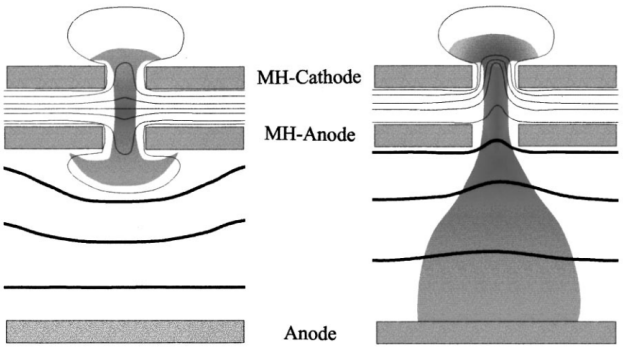

Figure 1.11: Diagram of the MHSD electrode configuration, featuring a second anode below a MHCD device. Left to right the MHCD is operated in the townsend and glow discharge regimes respectively, with the bias voltage of the second anode required to affect the MHCD plasma depending on the mode of operation. Reproduced from Stark *et al.* 1999.[85]

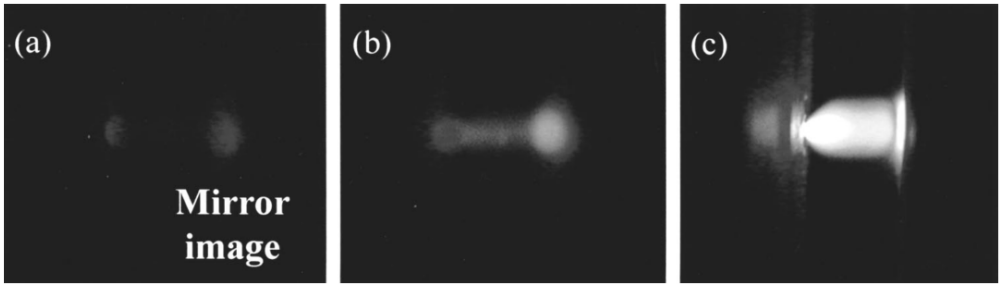

Figure 1.12: Photographs of MCSD glow discharges at currents of a) 1 mA, b) 1.46 mA and c) 4 mA. Reproduced from H. Park *et al.* 2003.[62]

model able predict properties of the plasma far from the electrodes, which was originally not possible with other geometries due to difficulties of separating the main body of plasma from the sheath structures near the electrodes. The ability to model the plasma separately from the MHCD device has allowed concentration on the plasma chemistry of MHSDs, specifically the mechanisms which allow efficient production of ($^1\Delta$) O_2 during operation of MCSDs in nobel gas-O_2 mixtures, with exciting biological appliation.[12,52]

1.6.5. Cathode Boundary Layer (CBL)

The Cathode Boundary Layer (CBL) geometry is operated using DC at atmospheric pressures consisting of ring shaped anode surrounding the negative glow shown in figure 1.13 (left), compared to planar anodes in MHCDs. The introduction of a ring shaped anode causes the negative glow to become a virtual anode, carrying both axial and transverse current, with the resulting discharge displaying a transition from a homogenous discharge to a discharge made up from localised points, shown as figure 1.13 (right).[78] Due to its positive V-I characteristics over its current range, arrays of CBL devices can be operated without the need for individual ballast resistors, shown in 1998 by Frame and Eden.[22] CBL devices have also been shown to emit excimer radiation of between

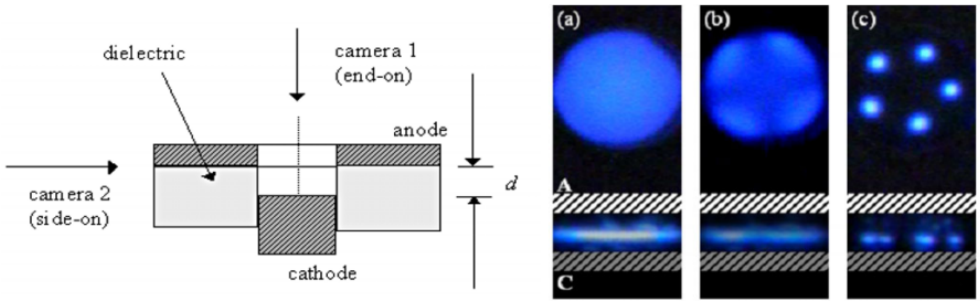

Figure 1.13: **Left:** Diagram of the electrode geometry of a CBL device. **Right:** Image of CBL discharges in 75 Torr Xe operated between 0.22 mA (left) and 0.09 mA (right), showing a transiton from a diffuse negative glow to localised regions at low currents. Reproduced from Schoenbach *et al.* 2016.[78]

1% and 9% luminious efficacy under medium and high pressure Xe, N_2 and AF gas,[59,81,82] making it another promising candidate for use in arrays for applications requiring the production of VUV radiation.

1.7. Materials

There have been a large range of different materials used for the construction of the cathode, anode and dielectric layers making up microdischarge devices in literature. The dielectric, which is responsible for shaping the electric fields within the devices are often made of materials with high dielectric constants, with a common choice of dielectric being mica sheet, a silicate mineral. Its insulating properties, machinability and inertnessallowingit to be used with a large range of discharge gases.[62,83] There are many other alternatives to mica such as polymers, Al_2O_3, alumina and other refractory materials; the latter proving to have many unique properties useful for specific applications while also being extremely hard and heat resistant.[7,20]

The electrodes and especially the cathode are often subject to both intense ion currents and temperature gradients. Molybdenum is a popular material due to its high melting point and resistance to sputtering. It is often used for high-current applications in form of a thin foil[45,82] or as a thicker (100 µm) layer.[68] Other, more machinable metals such as such as copper, silver and nickel have also been used in lower current applications.[92]

Silicon has also been adopted as a useful electrode material, mostly due to the already well established fabrication techniques such as ultrasonic or laser milling[22,23] and wet etching techniques allowing structures below 70 µm to be formed.[14] There has also been uses of silicon in the form of a reverse-bias pn junction, with the depletion zone replacing the dielectric.[94]

1.7.1. Diamond-based Microdischarge Devices

More recently, there has been interest in the use of CVD grown diamond in the construction of microdischarge devices. Diamond is extremely strong material with a high thermal conductivity

coefficient and melting point.[4] Its extremely low thermal expansion coefficient and is resistance to sputtering effects makes it ideal for the high power deposition applications involving large temperature gradients.[55,90]

Mitea *et al.* created an electrode-dielectric-electrode sandwich structured microhollow cathode device constructed solely from CVD diamond, using highly-boron doped diamond as the electrodes sandwiching an insulating intrinsic diamond dielectric.[55] Similarly Truscott, *et al.* created MHCD devices using an intrinsic CVD dielectric. However, only a single commercially grown boron-doped diamond electrode was used, with a separate annular molybdenum electrode included as part of a jig to hold the device acting as the anode. Breakdown and I-V characteristics were found to be comparable to conventional material devices in literature, with the etching mode of the diamond cathode was also studied.[90]

Hatta *et al.* used a boron-doped diamond electrode as the cathode of a parallel-plate macroscopic gas discharge due to the negative electron affinity of the hydrogen terminated diamond surface.[32] It was found that the b-doped diamond cathode reduced the discharge voltage compared to standard nickel and stainless steel electrodes. However, after 30 minutes of operation the discharge voltage increased due to sputtering damage by ions on the hydrogenated surface.[29]

1.8. Applications of Microdischarges

Microscopic discharges, operating at pressures approaching or exceeding atmospheric pressure, have been shown to exhibit properties and characteristics which are favourable for many applications. Investigations into I-V characteristics of devices allowing the creation of vast arrays of microdischarges and the development of geometries which can support higher volume plasmas. The introduction of arrays has allowed the previous volume limitations of microdischarges be overcome.

The ability for microdischarges to produce such non-thermal plasmas at atmospheric pressures, with high current and electron densities and with a non-Maxwellian electron energy distribution, favour excited species creation such as excimers. These characteristics make microdischarges potentially useful in sterilisation and environmental applications, especially destruction of pollutants, promoting chemical reactions and VOC destruction.[7,57]

1.8.1. Environmental Applications

Waste gas remediation using non-thermal plasmas such as processing NOx and SOx as well as the destruction of volatile organic compounds (VOCs) has been reality for over 20 years. However, the transition from laboratory based tests of microdischarge based solutions has been slow paced, due to issues including the lifetimes of such devices constructed from currently available materials and an insufficient understanding of finer details of decontamination reactions and their effectiveness.[7] Work by Koutsospyros *et al.* investigated three capillary electrode based reactors, finding that gains to efficiency can be made with increases to reactor volume, contaminant concentration and residence time of the gas in the chamber. However, efficiencies of contaminant destruction is reduced when present in mixtures of VOCs, suggesting that intermolecular interactions must first

be better understood.[7,40,41]

1.8.2. Trace Contaminant Detection

The use of microdischarges in chemical sensor applications have become an important area of research due the potential to create extremely compact low power devices. Detection of minute concentrations of both complex and simple molecules have been shown to be possible using a range of microdischarge devices. Microdischarges have been used to detect species though fluoresence measurements of the microdischarge, with the use of gas chromotography column in the case of complex mixtures.[7,54]

1.8.3. UV Radiation Sources

The range of wavelengths emitted by high pressure microdischarge devices due to the production of excimers can be extended deep into the ultraviolet region with efficiencies reaching 20% with ns pulse operation. The incorporation of small quantities of H_2 or O_2 also allow the production of UV line radiation rather than excimer continuum radiation.[45,84] Figure 1.14 shows the line radiation emission from a microdischarge operated in Ne with a small addition of H_2, allowing energy transfer from Ne_2^* excimers to form intense H Lyman α line emissions.[45,84]

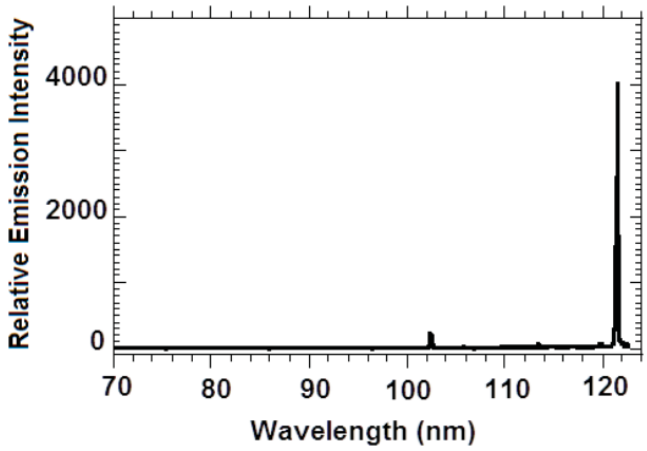

Figure 1.14: H Lyman α line emission due to the introduction of H_2 gas into Ne microdischarge. Reproduced from Kurunczi *et al.* 1999.[45]

1.8.4. Biological and Medical Applications

Microdischarges operating at atmospheric pressures offer simple designs and constructions, with dense high energy electron environments made possible without substantial heating of the surrounding gas, an advantage when applying plasma based sterilisation to heat sensitive tools. DBD have been a key microdischarge geometry in generating stable high pressure glow discharges for

sterilisation operated using RF.[36] However, introduction of Resistive Barrier Discharges (RBD) have allowed DC operation of glow discharges resistant to transitions to an arc.[48]

1.8.5. Plasma Reactors

There has been work into the creation of flow reactors incorporating a single microdischarge device. Chemical decomposition of NH_3 and CO_2 gases were observed though both electron and ion impact as well as thermal effects due to high gas temperatures of ~2000 K.[35] Qiu *et al.* designed a single MHCD based flow reactor for the conversion of NH_3 to H_2 for use in a portable fuel cell. With a maximum observed power efficiency of 11%, the use of microdischarges in plasma reactors needs further work, however incorporation of pulsed operation, higher concentrations of reactants and decreased flow rates may result in large gains in power efficiency.[7,71]

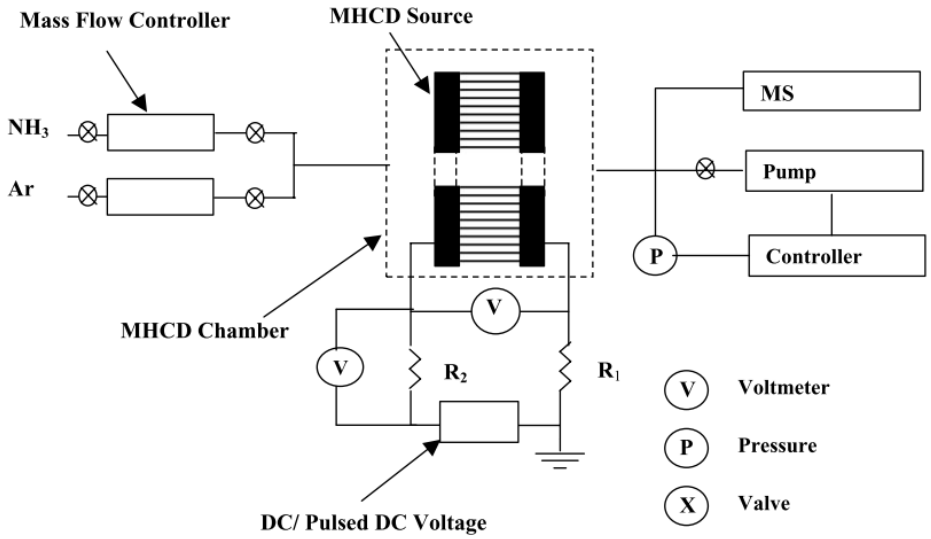

Figure 1.15: Schematic of a single MHCD flow reactor for the conversion of NH_3 in Ar to H_2 for use in fuel cells. Reproduced from Qiu *et al.* 2004.[71]

2. Experimental

2.1. Device Design

The device geometry and fabrication process was based on previous work by Truscott *et al.*, using the combination of an electrode-dielectric structure and an anode containing device holder in order to complete the electrode-dielectric-electrode sandwich structure shown in figure 2.1. The cathode material was varied between devices.[90]

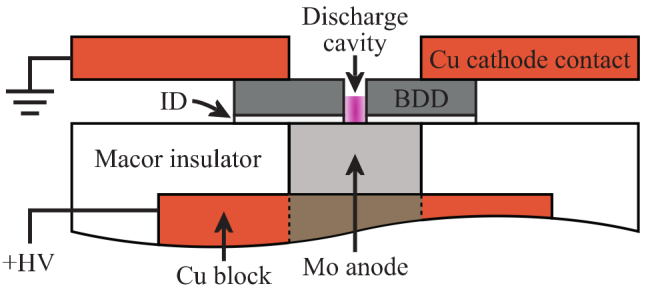

Figure 2.1: Schematic of a boron-doped diamond (BDD)-Insulating diamond (ID) device in conjunction with a macor constructed device holder containing a molybdenum anode. Reproduced from Truscott *et al.* 2016.[90]

2.2. Device Fabrication

Due to the anode being self-contained within the device holder during operation, the devices contained only the cathode and insulating dielectric layer, greatly simplifying the fabrication process to make it a two step process.

2.2.1. Cathode Material

The cathode of the microdischarge devices was made out of one of three materials: p-type silicon (B-doped), n-type silicon (P-doped) and highly boron-doped polycrystalline diamond (p-type) which was purchased from Element Six. All wafers were of dimensions 10x10x0.6 mm and could support four cathode hollow devices of dimensions: 5x5 mm.

2.2.2. Intrinsic Diamond Growth

A layer of insulating intrinsic diamond was grown onto one of the sides of the cathode wafers using microwave-plasma-activated chemical vapour deposition (MWCVD). Up to four 10x10x0.6 mm substrates could be inserted into the reactor during a single CVD growth run.

CVD growth was undertaken at flow rates of 300 and 19 sccm for H_2 and CH_4 respectively for 8 hours at 150 Torr and between 1.1 and 1.5 kW microwave power. The conditions were chosen to create an insulating diamond layer of between 40 and 50 µm thickness, however likely due to variations in substrate temperatures from the projected 900-950 °C average, growth rates did not reach 5 µm h^{-1}, resulting in a range of dielectric layer thicknesses ranging from 15 to 40 µm.

The dielectric layer thickness was measured after three CVD growth runs using SEM, also allowing the quality of the grown layer to be assessed. A SEM of a grown layer is shown in figure 2.2.

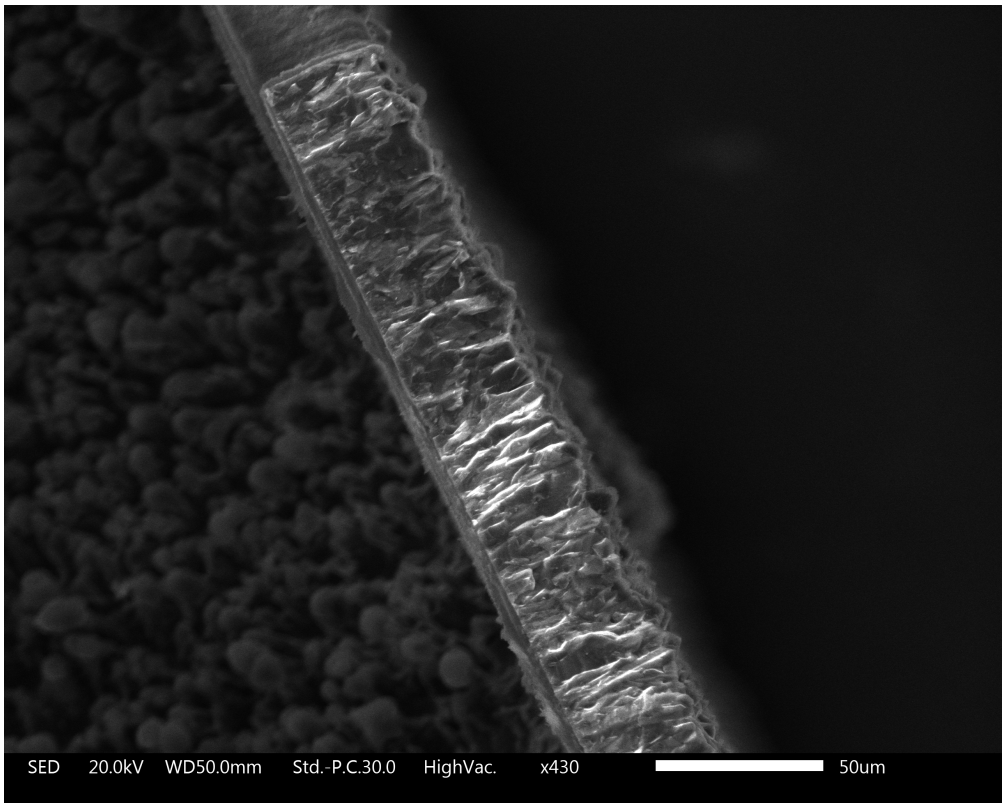

Figure 2.2: SEM image of a diamond substrate with MWCVD grown 40 µm intrinsic diamond dielectric layer. Variation in brightness between the two layers show differences in the relative conductivity and secondary electron yield of the layers, with insulating layers often appearing bright due to a build up of surface space charge from electron bombardment.

2.3. Laser Milling of the Hollow Cathode Structure

2.3.1. Milling Conditions

Silicon substrate samples were milled in a pure H_2 (~2 bar) environment, in order to reduce the formation of insulating silicon oxides and silicon nitrides on the cathode hollow surface. The high purity H_2 environment ensured that the the creation of Silane gas (SiH_4) during milling was the dominant silicon reaction mechanism, keeping the cathode hollow as free as possible from nitride and oxide species, which cannot be removed with common acids and bases. BDD substrate samples

were milled in pure O_2 (~2 bar) conditions, aiming to maximise the conversion of milled diamond into CO_2, rather than be redeposited as conductive graphite along the cavity surface or blocking up the milled hollow. In addition, the conversion of diamond to CO_2 is an exothermic process, increasing the peak temperature reachable at a given laser power, further increasing the milling speed achievable.[28]

The gas environments were created within a high pressure chamber containing a fused glass window and clip mechanism in order to hold the substrates in place during the milling process. The pressure chamber and substrate holder are shown in figure 2.3.

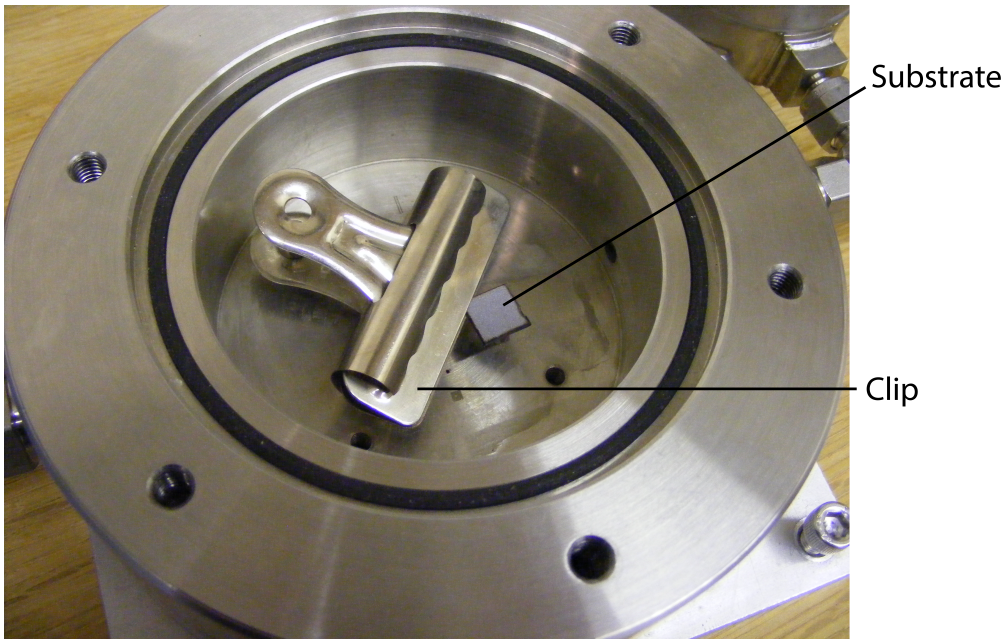

Figure 2.3: Picture showing a silicon substrate held in place at 1 corner using a clip, attached to the base of the high pressure chamber suitable for use with a laser cutter.

In previous work the 10x10 mm substrate-dielectric structures were split into four smaller 5x5 mm substrates, each containing a central cylindrical hollow; however it was found that the larger substrate could support all 4 separate microhollow discharge devices without need for separation, with each hollow able to be used separately through the use of an improved device holder, outlined below.

Once the two-layer, cathode-dielectric structure had been created, the hollow cathode structure could then be laser machined. The cylindrical hollow was milled using an Alpha series Nd:YAG micromachining laser (532 nm), manufactured by Oxford Lasers. The x-y translation rate during hollow creation was chosen to be $2\,\mathrm{mm\,s^{-1}}$, with a pulse spacing of 0.005 mm, in order to maximise the uniformity of the formed hollow. However due to time constraints, milling time was decreased though increasing the x-y speed to $10\,\mathrm{mm\,s^{-1}}$ and pulse spacing to 0.015 mm, resulting in a reduced milling time and increased cutting power respectively, with little decrease in the hollow uniformity. A rate of cutting in the z-axis of 2.5 µm/pass was chosen to be an overestimate for all silicon-based devices and roughly what would be expected in BDD based devices, making sure that all hollows were milled completely though both layers without requiring a second milling cycle from the other

side. Each hollow was milled central its corresponding quadrant on the 10x10 mm substrate, shown in figure 2.4. The method of determining the absolute position of the hollows for each substrate is shown in appendix A.

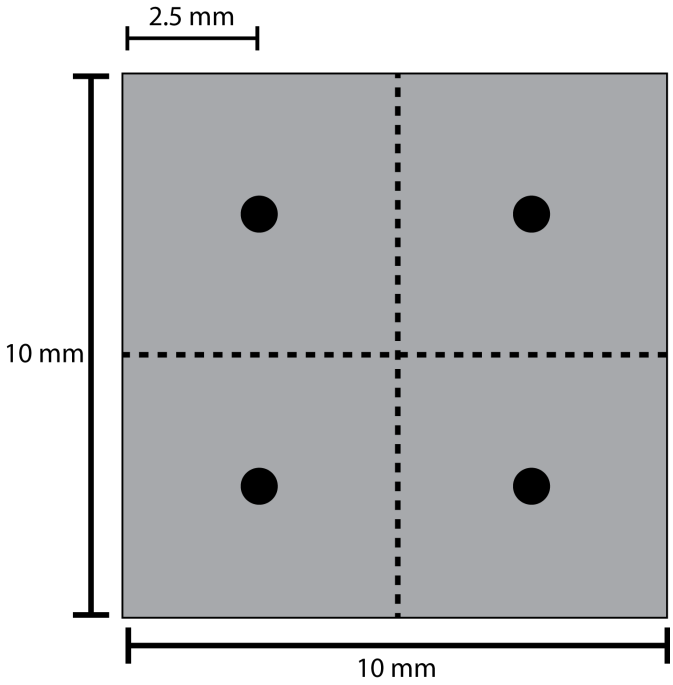

Figure 2.4: Schematic showing the positions of all 4 hollows milled into each 10x10 mm substrate.

It should be noted that for the milling of holes with diameters less than 200 µm, diffraction and beam divergence effects[15] sometimes resulted in the introduction of large deformities and non-uniformity in created 150 µm diameter hollows. It was noticed in previous studies that a cross pattern often appeared, requiring milling from both sides of the devices to achieve the required uniformity.[91] Drilling from both sides was only required in a limited number of cases, potentially due to the oxygen environment used for the milling of diamond, preventing a build up of graphite inside the hollow, which was not employed in prior work.

2.3.2. Cleaning of Devices

In previous studies, the formation of a conductive graphite layer on the surface of the BDD based devices during milling[11] and device operation, required an etching process of concentrated HNO_3 (16M) for˜2 hours.[37,91] By milling BDD devices in O_2, the formation of graphite during milling was significantly reduced, with the small amount formed removed through sonication in acetone or methanol for 15 minutes. The success of this process was confirmed using optical microscopy.

Silicon substrate devices were subject to melting, sputtering and due to trace O_2 and N_2 species, the formation of silicon oxide (SiO_2) and silicon nitrides (Si_3N_4) during both the milling and microdischarge operation. Silicon devices were sonicated, like BDD devices, in acetone or methanol for 15 minutes to remove these surface species.

2.4. Device Holder

Initial measurements of both silicon and diamond-based devices were undertaken using a device holder design described by both Alex Kershaw and Chris Turner, constructed from macor, a machinable ceramic insulator and containing a copper heatsink and an cylindrical molybdenum anode, chosen due to its high melting point and resistance to sputtering. A schematic of the device holder is shown in figure 2.5.[37,91]

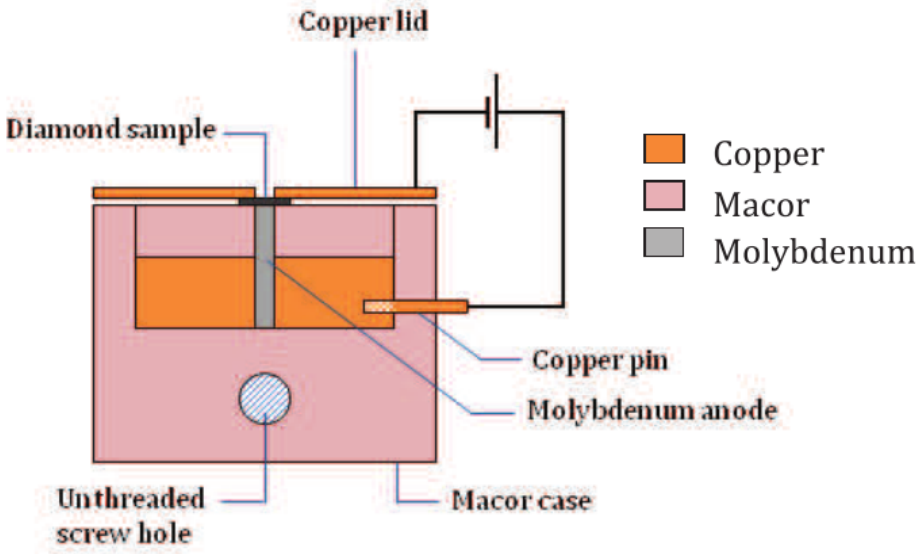

Figure 2.5: Schematic of the original device holder, constructed from macor and containing a copper heatsink connected to a annular molybdenmum anode. Reproduced from C. Turner, University of Bristol, 2013.[91]

Following on from initial designs and partial construction of a revised device holder by A. Kershaw, containing an improved device alignment mechanism and hollow copper anode, a second device holder was constructed. It contained more thoroughly insulated electrical connections to the copper lid and anode, while also containing a channel for convection currents to potentially remove sputtered material and graphite though the now hollow anode and out of the system.[37] A diagram of the holder's construction is shown in figure 2.6. The device holder itself it mounted to the flange of the high pressure chamber, equipped with airtight feed-throughs for electrical connections.

2.5. High Pressure Chamber

A stainless steel high pressure chamber with a capacity of ~0.5 L was used to conduct all microdischarge experiments, able to support gas pressures of up to 10 atm (7600 Torr). The chamber contained a quartz window which allowed the centrally-positioned device holder to be observed, with the microhollow visible through the hole in the device holder lid. The chamber was connected to a dual stage diaphragm pump including a Pirani gauge. The gas pressure within the chamber

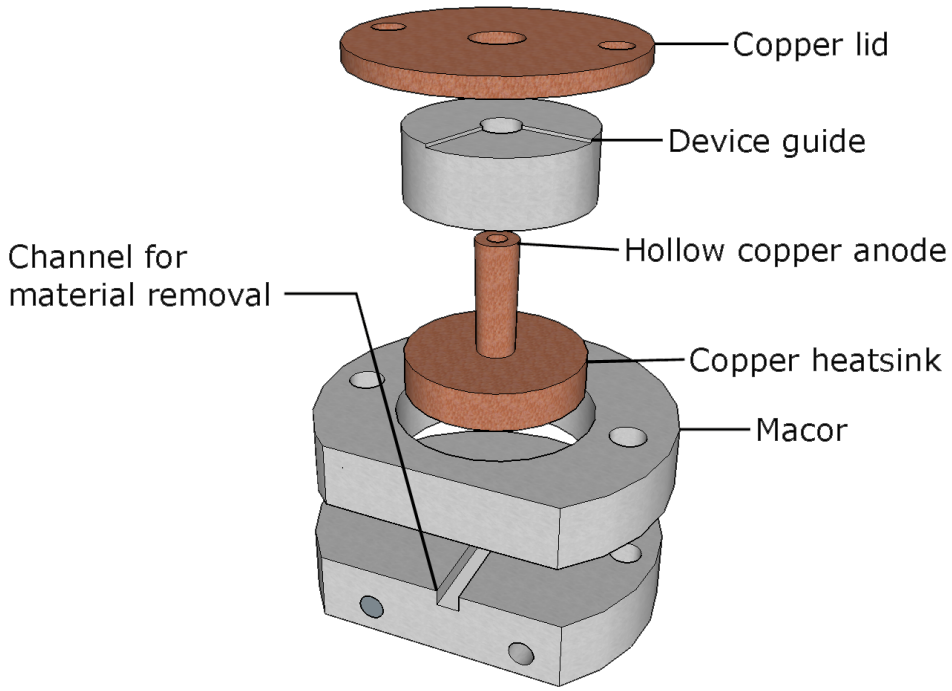

Figure 2.6: Diagram of the new device holder, containing a copper anode, channel for gas flow and a recessed square groove to allow for improved aligning of the sample hollow with the anode and the lid. Not shown: steel doweling to be inserted into the holes pictured, keeping the components of the holder together and providing anchor points for the lid.

monitored by a Kobold Man-SD3S pressure gauge (accurate to ±1%) and varied by an inflow of gas from connected gas cylinders (He, Ar) or from the lab gas lines (N_2) with the rate of the flow controlled by a needle value. A diagram of the gas inlet set up is shown in figure 2.7

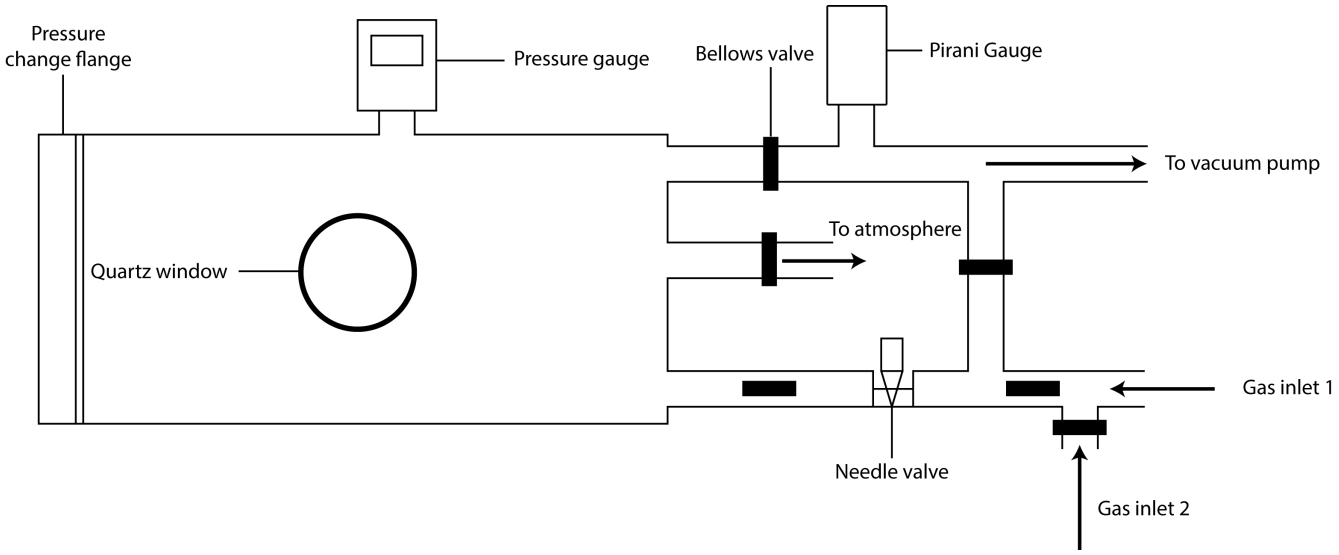

Figure 2.7: Diagram showing the gas set up for the high pressure chamber.

2.5.1. Electrical Set-up

The flow of current and the voltage across the electrodes was measured using two voltage probes connected to a LeCroy WaveRunner 64Xi oscilloscope, measuring V_high and V_low as shown in figure 2.8. The voltage across the microdischarge device was calculated from $V_{high} - V_{low}$ while the current was calculated using the voltage across a ballast resistor ($I = \frac{V_{low}}{R_{ballast}}$), which also served to reduce the power deposition by streamers and sparks which can damage the device. Initially a 4.68 kΩ ballast resistor was used in line with previous work,[37,91] however due to instabilities within the discharge, it was increased to 14.96 kΩ to suppress oscillations within the circuit.

The power supply used during all experiments was a Kepco BOP1000M high voltage power supply, capable of supplying ±1000 V and ±40 mA as both a current and voltage source. In order to produce the voltage and current waveforms required for breakdown and I-V behaviour studies and a Stanford Research Systems DS340 signal generator was connected to the power supply as well as the oscilloscope as a reference.

2.6. Device Operation

Before any measurements were made, the chamber was purged 3 times with the discharge gas, in order to minimise impurities from the air such as water and N_2 and O_2. Both N_2 and O_2 rapidly etch diamond and N_2 can react with silicon to form insulating silicon nitrides during operation of the devices.

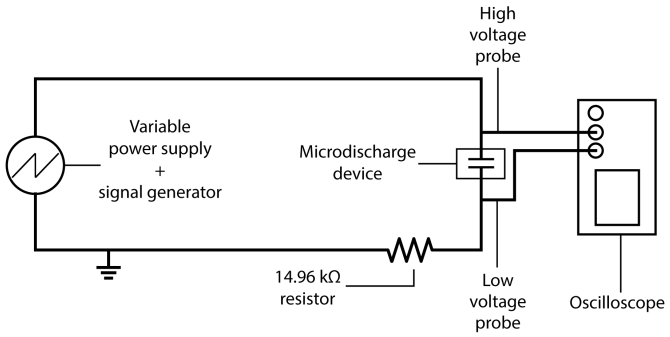

Figure 2.8: Schematic of the electrical set up for operating and measuring the breakdown and I-V curves of the devices.

2.6.1. Breakdown Voltage Measurements

In order to measure the breakdown voltage, the power supply was operated as a voltage source using a 1 Hz saw tooth wave, with a current limit applied. The voltage applied across the electrode increased until the breakdown voltage was reached, the voltage across the electrodes then dropped to the sustaining voltage and current flow could be seen on the oscilloscope. The amplitude of the sawtooth wave was constantly changed to ensure that the gas within the cavity was broken down with a current flowing for as little time as possible, reducing sputtering and heating effects on the devices. The current able to flow between the electrodes was limited to below 2 mA to limit erosion of the cathode surface, however in some cases this limit was raised in order to improve the stability of the breakdown and formed plasma.

The maximum voltage reached before the voltage drops to the sustaining voltage at breakdown was recorded by the oscilloscope and averaged over 30 ramping cycles in all cases. The standard deviation of the breakdown voltages across the sequence of voltage ramps was used as an error. Figure 2.9 shows the waveforms of the ramped current and the corresponding behaviour of the voltage measured by the oscilloscope.

Paschen curves for each device were produced by measuring the average breakdown voltage at a range of *pd* values, varied by changing the gas pressure and keeping the electrode separation fixed. In order to maximise gas purity throughout the breakdown measurements, breakdown measurements were made in two parts. First the breakdown voltage was measured with pressure incrementally decreasing from several atmospheres to vacuum, before a second set of breakdown values were measured with increasing pressure. In most cases, after 15 minutes sonication, a second set of descending and ascending pressure breakdown measurements were made. By measuring the breakdown voltages in this way, a much more complete dataset could be obtained, with much higher density of data compared to a single set of increasing or decreasing measurements. A plot of breakdown voltage against *pd* is shown in figure 2.10, using four separate data sets from ascending and descending pressure values.

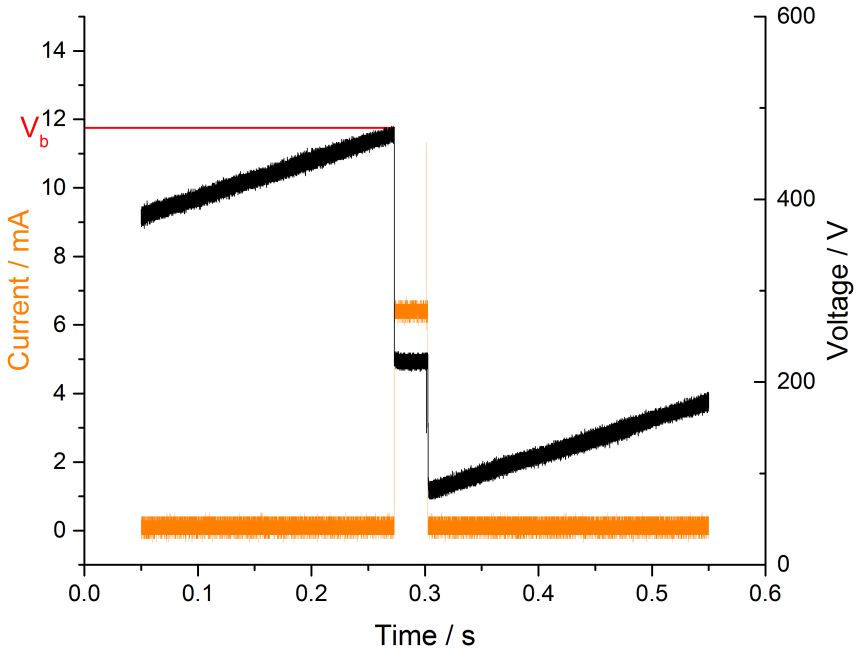

Figure 2.9: Oscilloscope waveform of both current and voltage for breakdown voltage determination using a sawtooth voltage waveform (black). The current has been limited to around 7 mA (orange) and is the amplitude and offset of the voltage sawtooth wave has been chosen so that a plasma forms within the cavity for only a fraction of a second, which can be seen in the short duration of the lowering sustaining voltage and non-negligible current flow.

2.6.2. Current-Voltage Curves

In order to measure the current-voltage behaviour for a range of devices, the power supply was operated as a current source, using a triangle wave to symmetrically ramp the current between 0 and ~15 mA. Again, using an oscilloscope the values of current and voltage were measured with respect to time and averaged 50 times.

Due to the computational power required to plot and manipulate the recorded voltage and current waveforms, a Sovitzky-Golay filter[76] was used applied to the current and voltage data. Using a decimation factor of 25, the number of data points was reduced from from 1,000,000 to 40,000 while it was confirmed that no detail was lost. A plot of the measured current and voltage behaviour with respect to time is shown in figure 2.11.

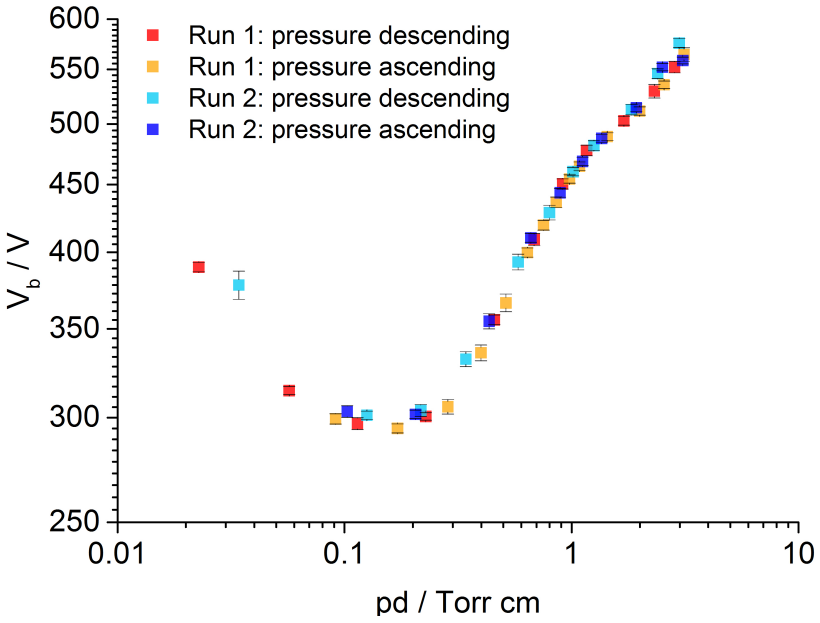

Figure 2.10: Plot of the breakdown voltage against *pd* for a p-Si device showing strong agreement between 4 ascending and descending breakdown measurements. The axes have been chosen to be logarithmic in order to focus on values of pd below 1 Torr cm

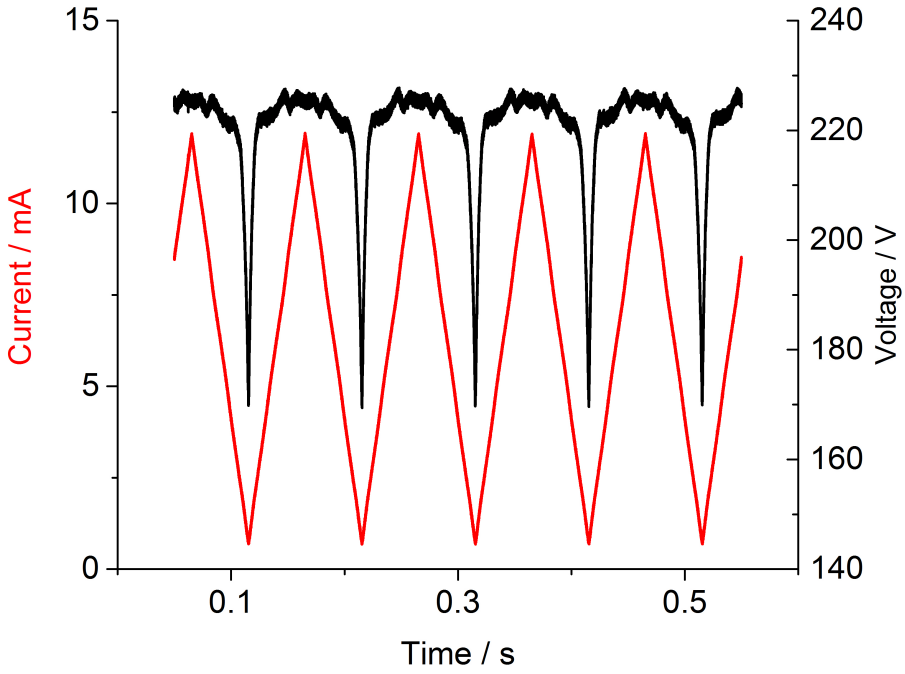

Figure 2.11: Plot of the ramped current (red) and resulting voltage values with respect to time. An I-V curve is constructed from plotting the voltage against the current.

3. Results and Discussion

3.1. The Thickness of the Intrinsic Diamond Layer

Microwave powers and reactant flow rates were kept as similar as possible between each growth run of 4 10x10 mm substrates in order to maintain a constant intrinsic diamond growth rate. However, most likely due to temperature differences between the substrates, the actual grown dielectric thickness was found to be highly varied.[1] After an 8 hour growth run containing two silicon substrates and 2 BDD substrates the dielectric layer on the BDD substrates were ~25 µm thick, much lower than previous substrate growth ((~40 µm). The p-type silicon substrate gained a 15 µm dielectric layer, consistent with all other p-type silicon substrate devices, indicating that that temperatures of the p-Si substrates were stable across multiple runs. The single n-Si substrate gained a significantly thicker dielectric layer of 30 µm compared to p-type silicon substrates, suggesting a higher substrate temperature, potentially associated with the quality of the thermal contact between the substrate and molybdenum cooling plate of the MWCVD reactor.

Additionally, BDD substrates were also subject to differing dielectric thickness between growth runs, varying from the predicted 40 µm range to thin 20 µm layers. In future work, it would be advantageous to subject only substrates of the same material to CVD growth during a single run, ensuring that individual substrate temperatures and therefore growth rates are as similar as possible.

As shown in figure 3.1, the thickness of the dielectric on p-Si devices (a) was around third of the predicted value, all being close to 15 µm, while devices based on a single n-Si substrate had dielectrics 30 µm thick (b). BDD diamond substrates (c and d) show a thick 40 µm and a thinner 25 µm dielectric layer respectively, which could also be due to differences in substrate temperatures stemming from thermal contact and microwave powers.

While the electrode separation (the dielectric thickness) is taken into account during breakdown studies, the aspect ratio of the discharges in devices of dissimilar dielectric thickness will not be comparable. The effect of the device aspect ratio was investigated by V. A. Lisovsky and S. D. Yakovin in 2000, finding that the breakdown voltage was not only dependent on the product of pressure and electrode separation *(pd)* as predicted by Paschen, but also of the ratio of the hollow radius to the dielectric thickness $\frac{d}{R}$.[50] While a difference of ~25 µm is small compared to the total thickness of the cathode layers, only the first few microns of the cathode will be active in the breakdown process and therefore the difference between a 15 µm and 40 µm dielectric is significant.

3.2. Breakdown Behaviour in Helium Gas

The breakdown behaviour of the samples was found to be similar to that of a parallel-plate electrode configuration, a curve containing a minimum on a $pd - V_b$ plot. For the majority of devices, two consistent breakdown behaviours were observed: one where the increase of V_b with increasing pd (right hand branch) was much steeper than predicted by Paschen's law and another where the right hand branch gradient was shallower and more comparable to a parallel-plate geometry. In all cases,

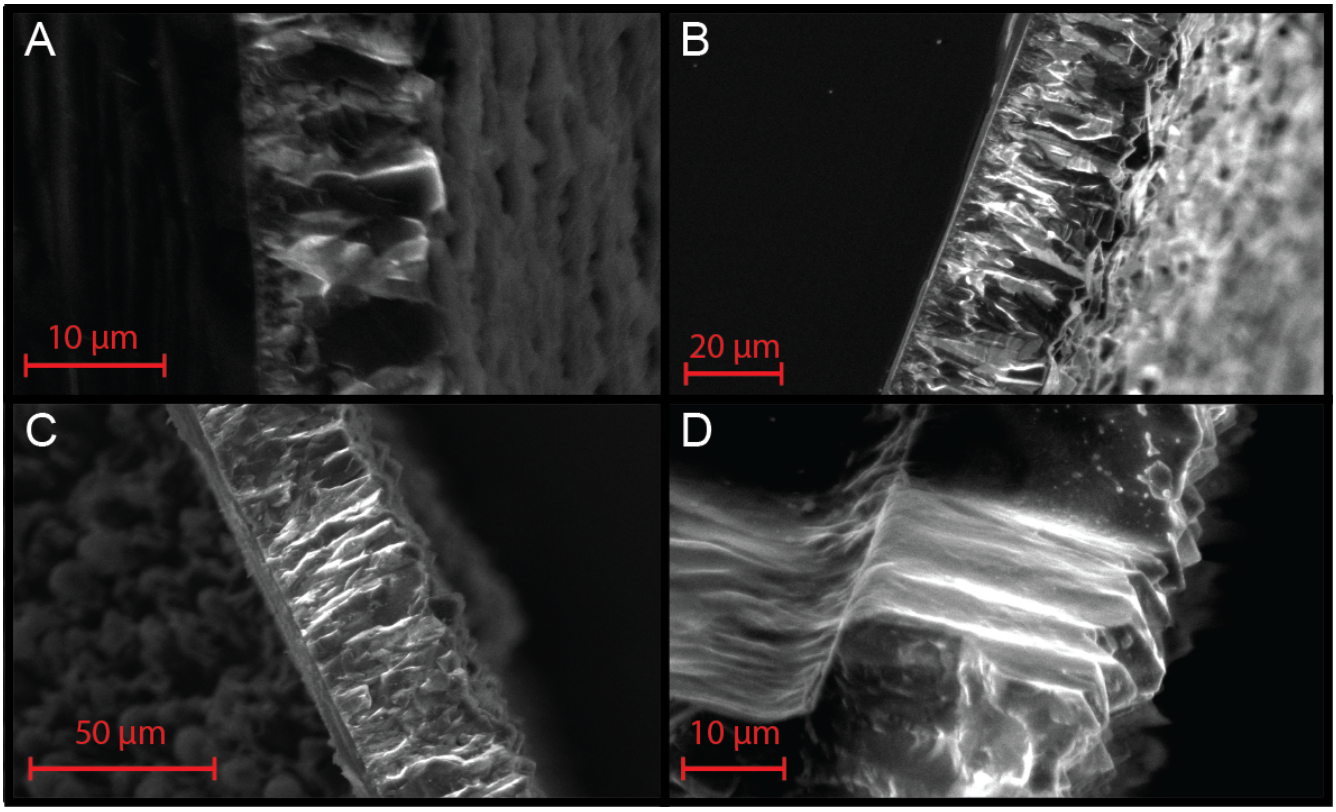

Figure 3.1: SEM images of four operated devices showing the thickness of the CVD intrinsic diamond layer. It appears lighter than the Si and BDD substrates due to a build up of space charge, however due to operation of the devices, some of the ID appears darker due to the presence of less insulating sputtered Si or graphite. **A:** p-type Si substrate with ~15 µm dielectric layer. **B:** n-type Si substrate with ~30 µm dielectric layer. **C:** BDD substrate with ~40 µm dielectric layer. **D:** BDD substrate with ~20 µm dielectric layer.

the breakdown voltage minimum was 150 to 250 V higher than that predicted for a parallel-plate configuration at the same electrode separation. Additionally, variation in breakdown behaviour between devices constructed to the same specification was often observed. Variation between separate measurement runs of the same device, suggests a rapidly changing cathode morphology during device operation.

3.2.1. Comparison of Observed Breakdown Behaviours

The breakdown behaviour over a range of He pressures for six different MHCD devices with both silicon and BDD cathodes, and a Paschen curve calculated from Paschen's law (equation 1) are shown in figure 3.2. The calcualted Paschen curve was plotted using He gas constants calculated by J. D. Cobine[16] and has been offset by 250 V in order to bring the parallel-plate breakdown voltages to similar values to those observed. The offset is thought to be partially due to the diffusive loss of electrons to the cathode walls at higher pressures.[50,90] The location of the minimum also occurs at a lower value of *pd* compared to the calculated Paschen curve, likely due to differences in

the electron mean free path between classical parallel-plate and microhollow cathode geometries. In the case of high pressure microhollow cathode geometries, the electron can be expected to undergo several collisions and become thermalised in much smaller distances than predicted by the geometry, moving equivilent parallel-plate predictions to lower values of *pd*.[90]

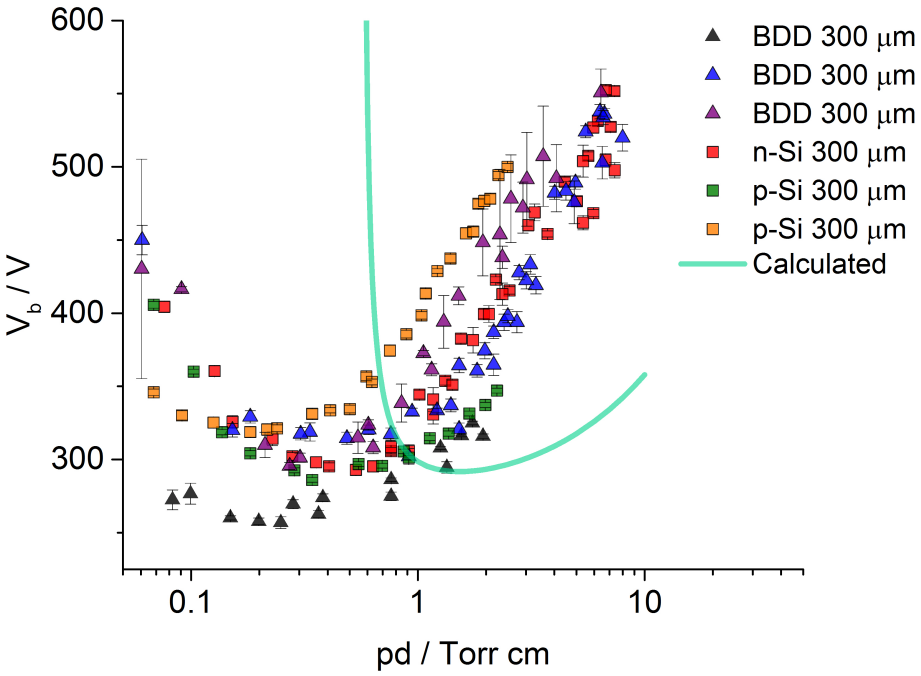

Figure 3.2: Breakdown behaviour in He of a range of devices containing 300 µm hollows in cathodes constructed from p and n-type Silicon and BDD diamond, compared with a calculated He Paschen curve with sodium-glass electrodes.[16]

The differences in the shape of the breakdown curves between the fabricated devices and that of the He Paschen curve cannot be explained through invoking differences in electrode geometry between MHC and parallel-plate, as similar devices have been shown to produce breakdown curves similar to those obtained for parallel-plate geometries.[37,90,91] Shown in figure 3.3 is the breakdown behaviour of 3 BDD microdischarge devices compared with a calculated He Paschen curve (the same as plotted in figure 3.2) by C. Turner, showing strongly contrasting behaviour to that produced in figure 3.2.[91] The main differences between plots shown in figures 3.2 and 3.3 is the gradient of the right hand branch compared to the calculated He parallel-plate Paschen curve. In figure 3.2 the majority of data follows a significantly higher gradient with increasing *pd* values, with only a few data sets following a lower gradient more similar to the calculated He Paschen curve in figure 3.3.

Figure 3.2 shows breakdown curves of devices tested multiple times in both high and low current conditions, while the more Paschen comparable figure 3.3 represents only a single run of measurements on newly fabricated devices. The deviation of breakdown behaviour from previous studies of the devices fabricated in this project suggests that changes to the internal structure of the cathode hollow and its chemical composition though repeated high current operation are important in determining a devices breakdown behaviour.

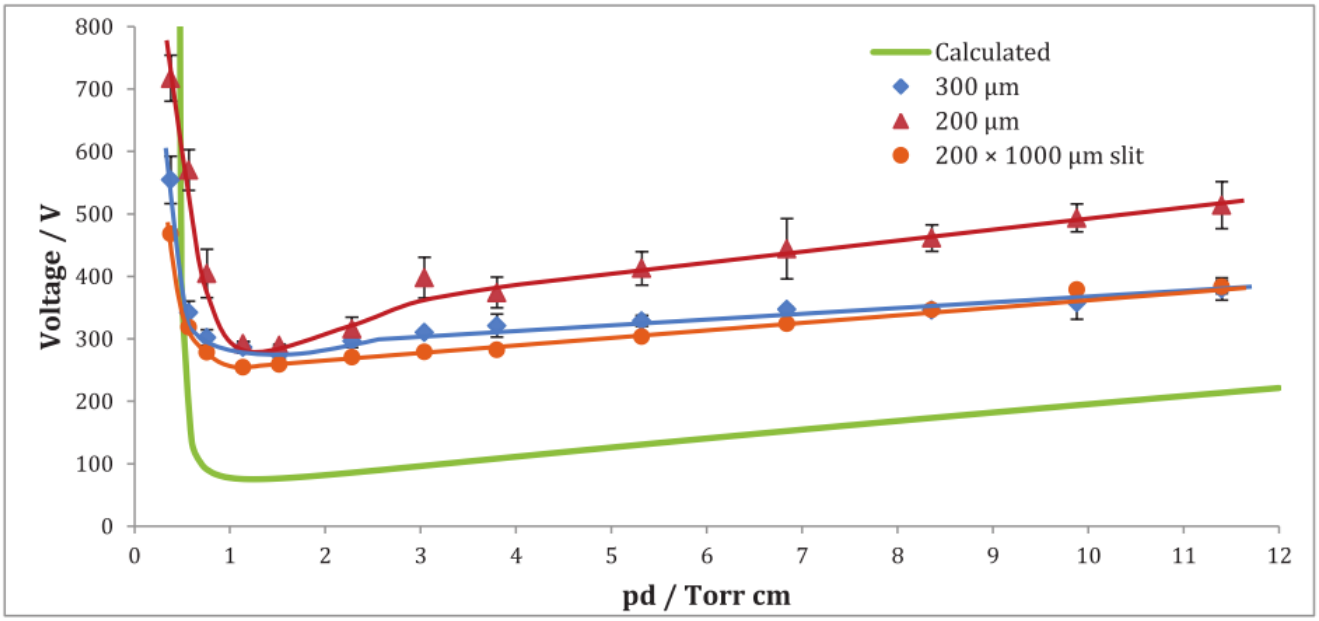

Figure 3.3: Breakdown curves of three BDD cathode MHCD devices of various hollow sizes and dimensions, compared with a calculated He Paschen curve. Reproduced from C. Turner, University of Bristol, 2013.[91]

3.3. The Effect of the Cathode on Breakdown Behaviour

3.3.1. Reliability of Measured Breakdown Behaviour

150 µm diameter hollows suffered from rapid changes to the hollow morphology during breakdown characterisation of both BDD and silicon substrate devices. An example of changing breakdown characteristics for a 150 µm device is shown in figure 3.4, where the breakdown voltage varied by 50 V for similar values of *pd*. These morphology changes include the formation and removal of microscopic protrusions on the cathode surface, also observed by Gomes *et al.* using molybdenum electrodes. A scanning electron micrograph (SEM) of the observed protrusions is shown in figure 3.5, these protrusions are expected to enhance the electric field surrounding them, temporarily lowering the breakdown voltage locally due to field emission.[26] In order to decrease the effect of varying hole morphologies compared to the hollow diameter, 300 µm diameter hollows were used for further breakdown measurements, with the added effect increased hollow morphology during the milling process.

3.3.2. Current Flow without Gas Breakdown

Through careful construction of the chamber and device holder, the breakdown voltage outside the microdischarge device was maximised, ensuring that any breakdown would occur solely within the device hollow. However, during operation in some BDD samples, a voltage drop was observed before the ramping voltage reached the breakdown voltage, as shown in figure 3.6. The voltage

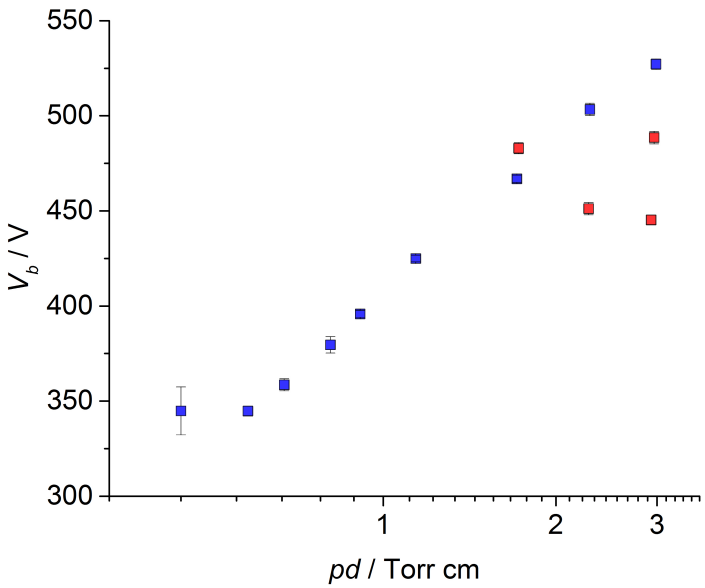

Figure 3.4: Breakdown behaviour of a n-type silicon cathode, 150 µm diameter device in He, showing variance of values during a single run of measurements.

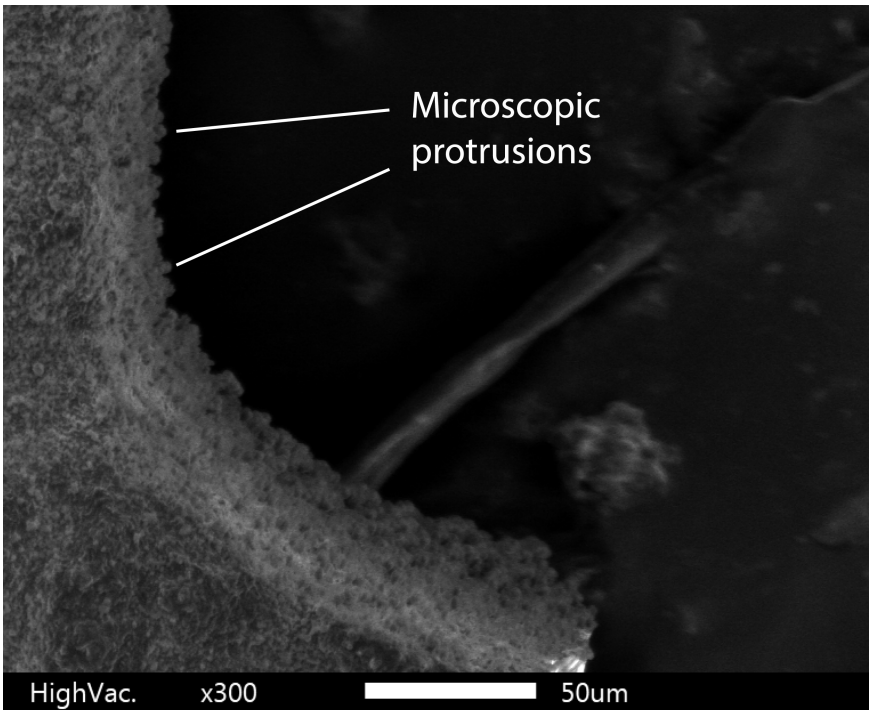

Figure 3.5: SEM image of the BDD cathode, showing microscopic protrusions formed due to the operation of a BDD substrate device.

drop, coinciding with a spike in current indicates that an alternate conducting path between the anode and cathode exists at lower voltages than the breakdown voltage of the microhollow. It is not clear whether this brief current flow exists within the device hollow as designed or via an

alternative path between the anode and cathode due to the breakdown of the insulating properties of the dielectric layer. However it is possible that because substrates contain multiple hollow cathode devices, the graphite on the cathode surfaces of other devices on the substrate could form a partial conductive path far away from the hollow of interest.

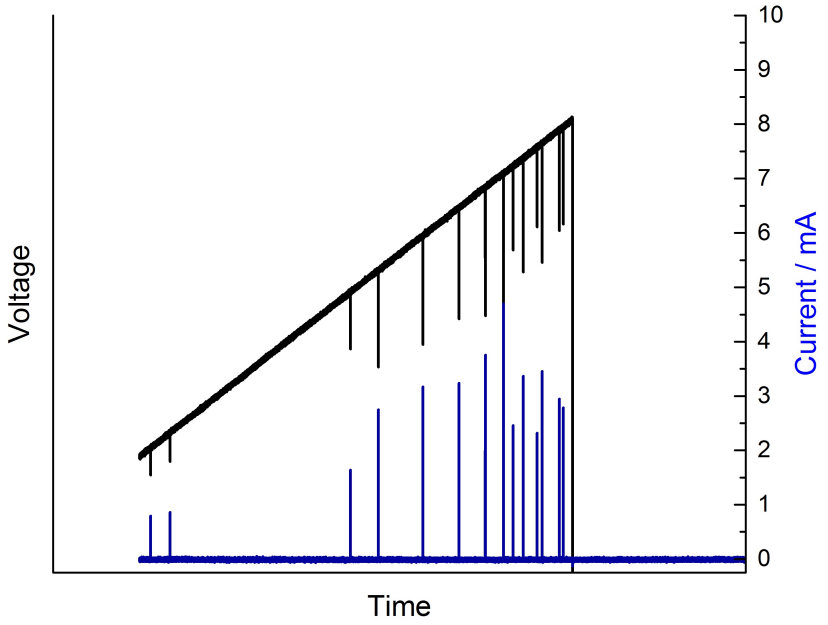

Figure 3.6: Plot of the voltage and current waveform during breakdown measurements of a BDD 300 µm device in Ar.

3.4. Changes in Morphology Between Breakdown Voltage Measurements

The breakdown behaviour of some devices was characterised multiple times, with some devices showing strong variation between runs, while others showed high consistency. The variation in the breakdown behaviour between different runs is shown in figures 3.7 and 3.8, two silicon substrate devices in He which produced the largest variations. This variation of behaviour between measurement runs occurred predominantly in silicon substrate devices, but was present in a limited set of BDD substrate devices which were characterised multiple times.

Figure 3.7 shows the breakdown behaviour recorded for one device over three breakdown measurement runs, separated by a sonication cleaning step in methanol to remove any loosely held material on the cathode surface as a result of sputtering and deposition processes. It can be seen that between the first and subsequent two runs, there is a definite change in the breakdown behaviour with increasing pressure (and therefore pd).

Possible changes to the silicon discharge devices and discharge conditions between runs are as follows: changes to the morphology of the hollow, changes to the chemical composition of the

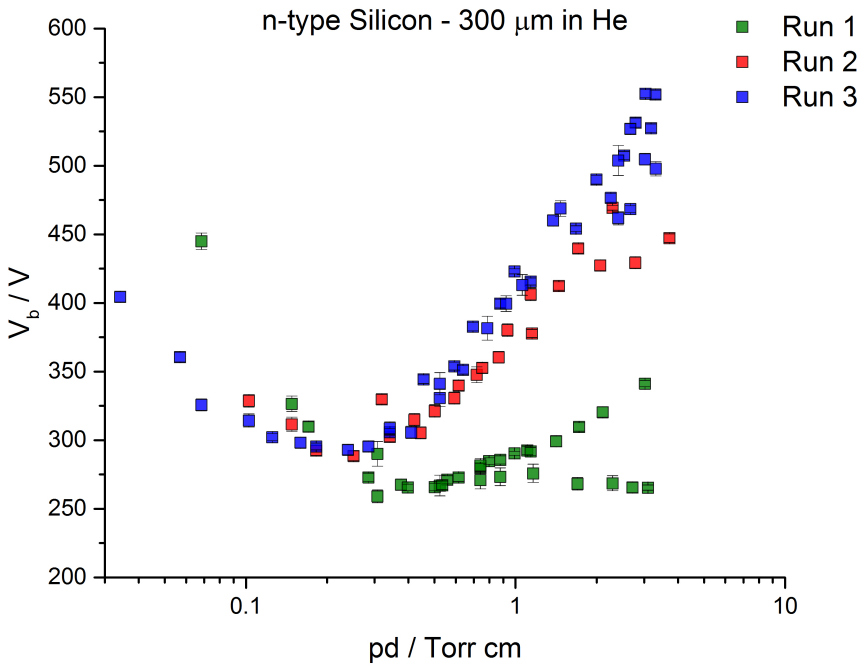

Figure 3.7: Breakdown voltage against pd for a n-type silicon cathode,300 µm device in He gas taken over three separate runs.

cathode hollow's surface and differences in discharge gas composition. M. Kulsreshath *et al.* found sputtering by He and Ar ions on the cavity surface were found to create a porous surface structure during operation of silicon substrate microdischarge arrays. Energy-Dispersion X-ray spectrometry (EDX) showed that the porous surface was soley deposited and melted silicon.[42] The formation of this porous surface was attributed predominantly to "transient micro-arcs".[56] The re-deposited silicon would likely be less highly doped after sputtering, affecting the secondary electron emission and conductivity of the surface.

Due to the presence of N_2 and O_2 impurities from atmospheric air, the formation of SiO_2 and Si_3N_4 species on the surface is also expected. However, the quantities required to produce a meaningful change in discharge properties are not known. Nonetherless, the presence of insulating nitrides and oxides of silicon would be expected to have a lower secondary electron yield than extrinsic silicon, which would result in a decrease in electron production from ion bombardment, increasing the breakdown voltage. The presence of N_2 and O_2 would also increase the breakdown voltage due to variation in their respective gas constants,[31] Purging of the discharge chamber should minimise concentrations of atmospheric air and water within the high pressure chamber, rendering their contributions to breakdown negligible. Divergence of behaviour within the first run itself (green) suggests that initial changes in morphology occur within the first stages of breakdown characterisation measurements.

While device operation often resulted in steeper breakdown behaviour in subsequent measurement runs, changes to breakdown behaviour was not always consistent, as shown in figure 3.8. The current flow limit of the power supply was changed between measurements in order to move the

discharge away from the unpredictable self-pulsing regime, resulting in the discharge devices being subjected to different power depositions during a single breakdown measurement run. The rate of both surface composition and morphology changes is likely highly dependent on the current density and power deposition within the cathode hollow, due to main mechanisms of surface modifications being heating, ion bombardment and microdischarge

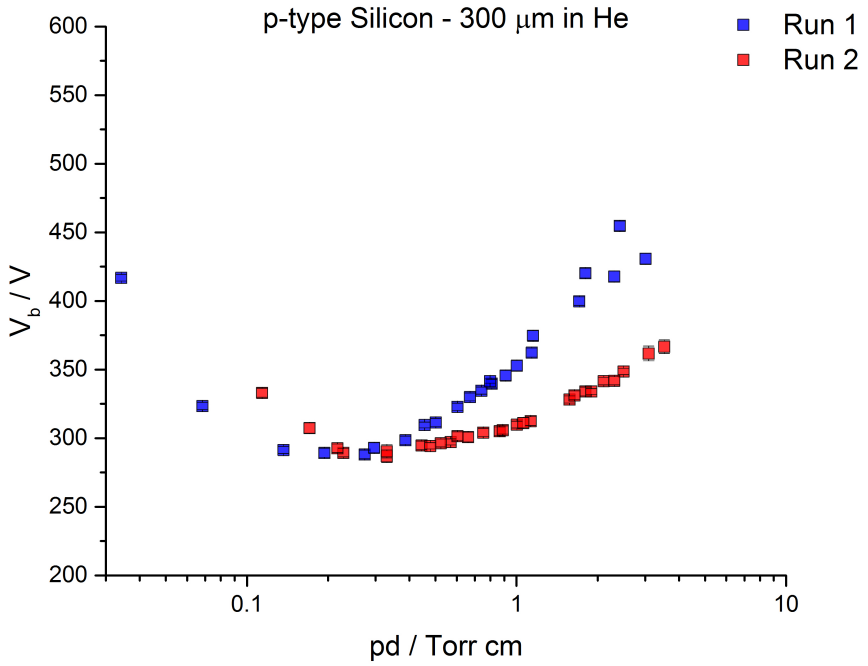

Figure 3.8: Breakdown voltage against pd for a p-type silicon cathode, 300 µm device in He taken over two separate runs.

Some devices failed to ignite at applied voltages far above the breakdown voltage, often taking minutes to start discharging. Once the discharge had been initially ignited, the device was then able to breakdown at a much lower breakdown voltage, in-line with breakdown voltages at similar *pd* values. The number density of seed electrons within the cathode cavity has an important effect on the field required to produce a self-sustaining electron avalanche,[69] A layer of passivating silicon nitrides and oxides in the case of silicon substrate devices would reduce the number of these seed electrons produced at the cathode photoelectically, while sputtering damage to the hydrogen termination of the BDD cathode surface would have similar effect in BDD devices, by removing the surface's negative electron affinity.[29] The reduction in seed electron number density would prevent striking of the devices only once the electron density stochastically reaches densities able to support self-sustaining electron avalanches, with the electron density maintained between voltage ramps due to slow diffusion of electrons produced during the discharge from the cavity. The sawtooth voltage waveform was kept positive at all times to prevent electrons being rapidly drawn back to the cathode between voltage ramps, preventing repeated striking issues from interfering with averaging by the oscilloscope.

A SEM image of the cathode cavity surface after high and low current operation in Ar and He environments is shown in figure 3.9. It can be seen that the surface of the silicon cathode has

become porous, through the deposition of silicon nitrides and silicon oxides coupled with sputtering and re-deposition of silicon and melting of the silicon surface. It was not possible to determine how quickly the silicon cathode becomes porous, as devices had to be bisected in order to view the hollow interior, making them inoperable. The porous surface will be less conductive than the original surface, due to the lessened conductivity of less highly doped re-deposited silicon and the presence insulating SiO_2 and Si_3N_4. It can also be seen in figure 3.9 that large particles of deposited material were formed, which can block the hollow or be removed, causing changes to behaviour before and after sonication.

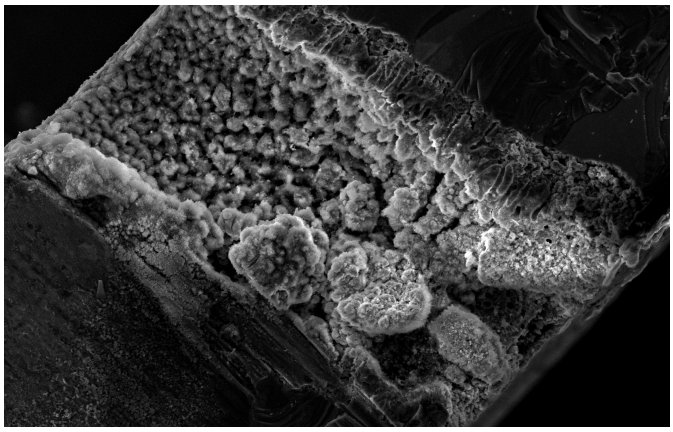

Figure 3.9: SEM image of a p-Si substrate device which has undergone severe sputtering of cathode surface, resulting in the deposition of insulating and less conductive silicon species as well as large surface structures which could be dislodged during cleaning.

3.4.1. Comparison of Morphologies And Their Breakdown Behaviour

The surface of the cathode hollows for two separate p-Si substrate devices were imaged using SEM (figure 3.10). Device 1 (left) shows a porous surface, constructed from sputtered silicon and predicted silicon nitrides and oxides. These surface features were most likely formed during high current I-V studies which often resulted in current densities of over $10\,\mathrm{kA\,cm^{-2}}$ inside the cathode cavity, in addition to higher density streamers. In contrast, device 2 (right) shows a relatively smooth, deposition free cathode cavity, due to operation at limited current densities in He, which sputters silicon less strongly due to its atomic mass. Device 1 showed a steep, non-Paschen-like right hand branch while device 2 showing a more shallow right hand branch more similar to the calculated parallel-plate Paschen curve and those obtained by Truscott *et al.*.[90] As previously discussed, the formation of insulating species on the surface of the silicon cathode reduces the conductivity and secondary electron emission of the surface compared to raising the voltage required to produce sufficient ion concentrations, compared to a relatively pure, doped silicon surfaces present in device 2 (figure 3.10 right). However, addition of insulating species to the silicon cathode surface does not provide an explanation as to why differences in breakdown voltage appear only at higher *pd* values with the breakdown of such devices very similar close to the minimum.

Comparison of the breakdown behaviour of BDD substrate devices showed an offset of breakdown

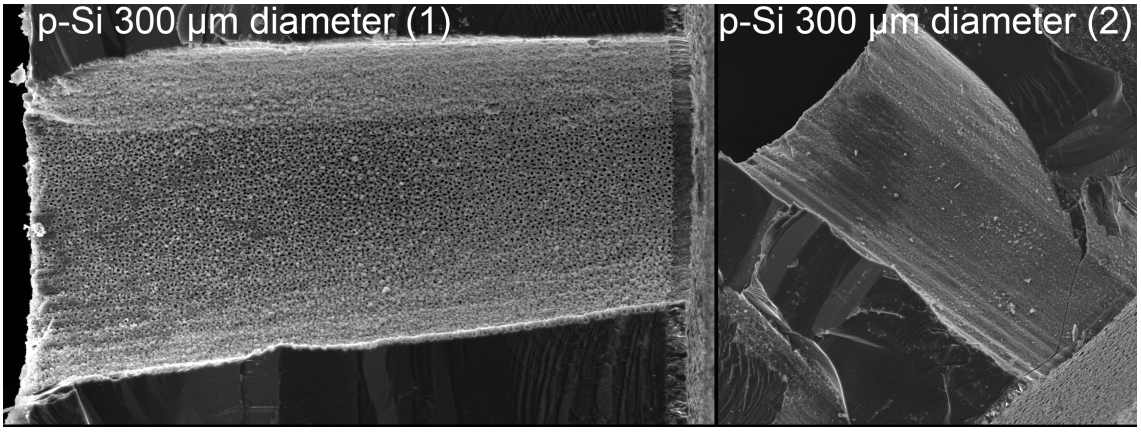

Figure 3.10: SEM images showing the morphology of the cathode surface within the device cavity. **Left:** p-Si device which showed a steep right hand Paschen curve branch with a porous silicon surface caused by the re-deposition of sputtered or melted silicon. **Right:** p-Si device which showed a more shallow right hand branch comparable to the calculated He Paschen curve, potentially caused by a relatively smooth surface free from insulating surface species due to limited use at high currents.

curves between different devices, rather than the changes in gradient observed for silicon devices (figure 3.2). During the process of sputtering by He and Ar ions, the negative electron affinity hydrogen terminated surface can be damaged, resulting in a reduction in secondary electron emission, which could explain the increase in the breakdown voltage for subsequent breakdown measurements.[29] BDD diamond cathode devices undergo erosion the cathode surface which is then removed as graphite, compared to silicon devices where the material remains as part of the cavity wall. Due to the similarity of Ar and C atoms, Ar etches diamond more strongly than He, but with sufficient current density and operation time, significant etching of the cathode can still occur in He gas. The action of He and Ar ion bombardment is shown in figure 3.11. Device 1 (left) was operated in high current conditions in Ar and He gas while device 2 was operated at high currents solely in He (right). The cathode material removal by Ar and He was found to extend the cavity to larger diameters and in the case of device 1 (figure 3.11, left), only the surface of the cathode able to support the glow discharge was eroded. After a secondary cavity of significant diameter had been formed, the glow discharge was often hidden from view outside the device preceded by a reduction viewing angle of the glow discharge. Device 2 (figure 3.11, right) was only operated in He, experiencing less significant etching of the cathode surface. However, this could be a combination of both the limited sputtering potential of He atoms and decreased current densities due to the increased available surface area of the cathode, resulting in reduced and more uniform cathode erosion.

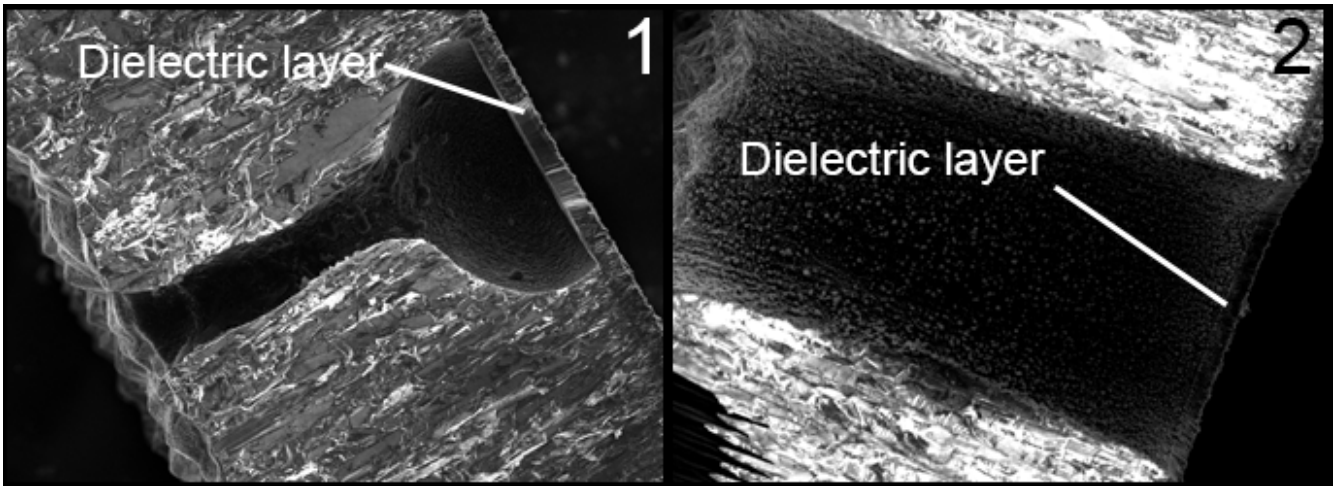

Figure 3.11: SEM images of the hollow cathode cavities of two boron-doped diamond substrate devices. **Left:** Heavily etched cavity in the BDD cathode due to operation in He, Ar and H_2. **Right:** Operation in only He has limited sputtering and etching effects compared to Ar of the BDD cathode cavity surface.

3.5. Fitting Breakdown Curves in Helium to a Modified Paschen's Law

In order to quantify the differences between the two behaviours observed for BDD and silicon cathode devices, Paschen's law for parallel-plate electrodes was fitted to the breakdown data for four MHC devices, allowing the gas constants A, B and γ to be determined. While Paschen's law doesn't apply to hollow cathode geometries and the empirical constants relate to the gases only, finding the differences in these gas constants between devices might offer clues into the processes involved in the breakdown mechanism.

Fitting was done using a non-linear least-squares minimisation of a Paschen's law modified to include offsets in both the pd and V_b axes. Four breakdown datasets of 4 different devices were fitted, corresponding to two BDD cathode and two p-type silicon cathode devices. Curves from the the same cathode material were plotted simultaneously, with some variables fitted to be constant across the two curves. The modified Paschen's law is shown in equation 2:

$$V_b = y_0 + \frac{B \cdot (pd - x_0)}{\ln(A \cdot (pd - x_0)) - \ln\big(\ln\big[1 + \frac{1}{\gamma_{se}}\big]\big)} \tag{2}$$

Where x_0 and y_0 are offsets in the pd and V_b axes respectively.

Both pairs of breakdown data, grouped though the devices cathode material, were fitted with the best fit values of γ, x_0 and y_0, held constant between the pair of curves. The best fit values of A and B were fitted independently. As a result, each curve of the pair was assigned individual values of A and B, while values of γ and the axis offsets were shared between the pair. Device 1 of the pair (e.g BDD Cathode 1) was plotted using equation 3.5A and Device 2 (e.g BDD Cathode 2)

using equation 3.5B:

$$V_b = y_0 + \frac{B_1 \cdot (pd - x_0)}{\ln(A_1 \cdot (pd - x_0)) - \ln\left(\ln\left[1 + \frac{1}{\gamma_{se}}\right]\right)} \tag{3.5A}$$

$$V_b = y_0 + \frac{B_2 \cdot (pd - x_0)}{\ln(A_2 \cdot (pd - x_0)) - \ln\left(\ln\left[1 + \frac{1}{\gamma_{se}}\right]\right)} \tag{3.5B}$$

where A_1 and A_2 are the values of A for devices 1 and 2 respectively.

The fitted curves and the breakdown data is shown in figure 3.12, with both BDD cathode device breakdown curves shown on the left (A), and both p-Si cathode device breakdown curves shown right (B). The best fit values of the constants in equation 2 are shown in table 1, where the value of A for "BDD Cathode 1" refers to the value of A_1 during simultaneous fitting. Values for parallel-plate measurements in He and Ar (entries 1-2) and best fit values by Truscott *et al.* for 3 BDD substrate device breakdown curves (entries 7-9) are included in table 1 for comparison.

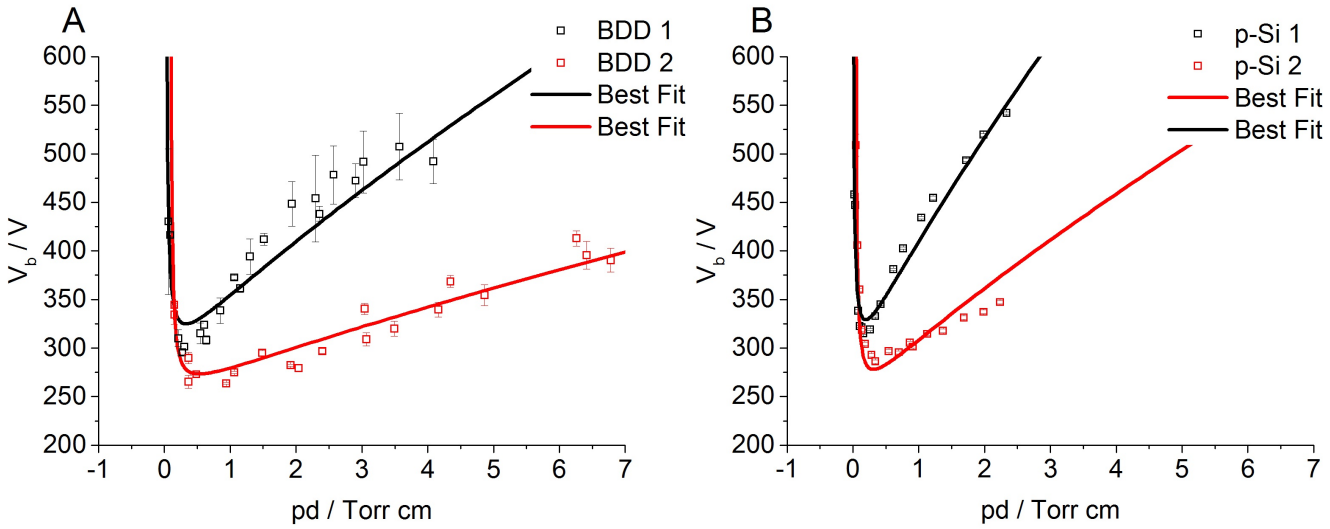

Figure 3.12: **A:** Best fits of two BDD cathode device breakdown curves using equations 3.5A and 3.5B, with the value of γ and the axis offsets consistent between them. **B:** Best fits of two p-Si cathode breakdown curves using equations 3.5A and 3.5B, with the value of γ and the axis offsets consistent between them. The best fit values are shown in table 1 (entries 3-6).

	Device	A / $\mathrm{Torr^{-1}\,cm^{-1}}$	B / $\mathrm{V\,Torr^{-1}\,cm^{-1}}$	γ	pd offset / Torr cm	V_b offset / V
1.	He parallel-plate[16]	2.8	34.0	0.263		
2.	Ar parallel-plate[16]	10.20	176.27	0.095		
3.	BDD Cathode 1	4.12	224	0.879	0.171	212.6
4.	BDD Cathode 2	2.94	86.4	0.879	0.171	212.6
5.	p-Si Cathode 1	45.9	452	0.00407	0.131	182
6.	p-Si Cathode 2	33.6	216	0.00407	0.131	182
7.	BDD Cathode 3 (200 µm)[90]	3.62	110	0.0532	0.591	72.5
8.	BDD Cathode 4 (300 µm)[90]	2.48	39.4	0.230	0.369	220
9.	BDD Cathode 5 (Slit)[90]	2.47	58.1	0.240	0.393	153

Table 1: Table of the Paschen's law parameters for a parallel-plate geometry in He and Ar (entries 1-2), best fit parameters for breakdown curves of BDD and p-Si cathode devices (300 µm hollow) operated in He gas from figure 3.12 (entries 3-6) and best fit parameters for 3 similar BDD hollow cathode devices, also operated in He, reported by Truscott *et al.* (entries 7-9).[90]

3.5.1. Correlation of Gas Constants and Their Physical Consequences

A and γ are strongly correlated, indicated by the correlation table (table 2) and equation 3, formulated by A. Von Engel,[93] showing the combined effect of A and γ on $(pd)_{min}$. In turn, B affects the value of the minimum breakdown voltage (equation 4), which is itself dependent on the value of $(pd)_{min}$, making all three constants highly correlated in their effect on the breakdown curve shape.

$$(pd)_{min} = (\frac{2.72}{A})\ln(1+\gamma^{-1}) \tag{3}$$

$$(V_b)_{min} = B(pd)_{min} \tag{4}$$

	A	B	γ	pd offset	V_b offset
A	1	0.0745	1	0.991	0.314
B	0.0745	1	0.0745	-0.109	-0.911
γ	1	0.0745	1	0.991	0.314
pd offset	0.981	-0.109	0.991	1	0.476
V_b offset	0.314	-0.911	0.314	0.477	1

Table 2: Correlation table of the constants in the modified Paschen's law, generated in Mathematica during a least squares fit of breakdown data for device: p-Si Cathode B.

The steeper gradient of the right hand branch of the breakdown curves for both cathode materials has resulted in increased values of A and B. The relative increases to A and B are also similar across both devices, around a 40% increase between A values and 250% between B values. Increases to both A and B correspond to reductions in the mean free path. Physically, the indicated decrease

in mean free path could be due to reduction of long path breakdown probability, with progressive morphology changes restricting breakdown to electrons emitted from the cathode at distances closer and closer to the anode. The porous surface of the cathode in the case of silicon cathode devices and eroded hollow in BDD cathode devices could be enhancing the diffusion of secondary electrons away from the cathode cavity, raising the breakdown voltage.

In comparison to γ values calculated for the parallel-plate sodium glass electrodes (figure 1, 2.), best fit values of γ (entries 3-6) are very high and very low for BDD diamond and silicon cathode devices respectively. γ is dependent on not only the gas but also the electrode material and its geometry, with the former being the same across all devices. High values of γ correspond to higher probabilities for a secondary electron to be emitted from the cathode due to impact by a gas atom. One reason why the BDD cathode might exhibit high values of γ compared to silicon and sodium glas could be due to the negative electron affinity of hydrogen terminated BDD.[29] Similarly, a low value of γ could indicate a cathode surface with a low probability of election emission, due to its porous morphology and chemical composition. As a result of correlation between A and γ, reductions in the value of A, especially in the case of p-Si cathode devices can allow γ to be increased to values exceeding 1, while maintaining good accordance between the experimental data and fitted curves. Hence, values of γ, while being an important metric in analysis of changes to the cathode surface, cannot be relied on independently. Attempts were also made to fit breakdown curves with best fit values of A and γ, or B and γ differing between the devices. However, achieving physically reasonable best fit values was not possible in the case of A and γ differing between devices, due to their high correlation.

3.6. I-V Behaviour

The Current-Voltage behaviour for a range of devices and pressures were measured, giving insight into the form of the discharge after successful breakdown of the gas. It was common for I-V results to be strongly spread, with repetition of measurements required to record relatively smooth I-V curves. The large variation, which hid many features of the I-V curve, were due to instabilities in the glow discharge, such as streamers and short lived arc discharges from the hollow to the copper lid. The shape of the I-V curve offers insight into the current density and spatial evolution with increasing current flow of the plasma as well as qualitative comparison with literature.

Schoenbach *et al.* recorded the first I-V curves of a MHCD with thin molybdenum electrodes separated by a 250 µm mica dielectric, as shown in figure 3.13. There are three key regions present: the Townsend dark discharge and the normal and abnormal glow discharges. The Townsend regime exists from 0 A until label 'a', where it transitions to the glow discharge at label 'b'. As the gas becomes more and more ionized with increasing current, the voltage required to sustain the plasma drops and the plasma expands to cover more and more of the cathode surface. At 'd', the rise in voltage signals an increase in current density due to complete covering of the cathode surface and the I-V curve enters the positive differential resistance abnormal glow. The presence of a positive differential resistance means that MHCDs such as those tested by Schoenbach *et al.* can be operated in parallel without the requirement of individual ballast resistors, making them highly favourable in array applications.[80,83]

The I-V characteristics of many MHCD devices measured were found to be highly unreproducible,

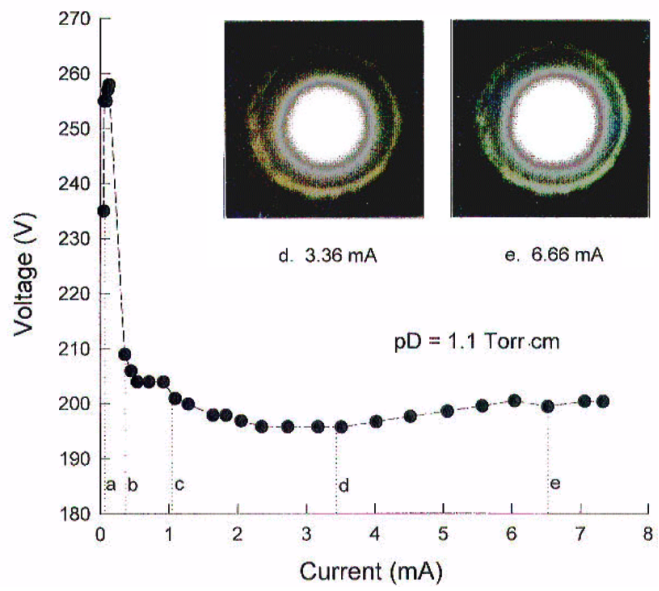

Figure 3.13: Diagram of the current-voltage characteristics of a MHCD device (200 µm diameter) in 56 torr Ar investigated by Schoenbach in 1997. Also included are CCD images of the plasma during operation.[80]

due to ohmic contributions from graphitization of the cathode and dielectric surfaces, changing interior morphologies and the formation of streamers across the outer cathode surface to the lid. Displayed in figure 3.14 are I-V curves measured for p-Si and BDD cathode devices in Ar and He, that best I-V behaviour observed for a large number of devices while being free of voltage fluctuations. The I-V curves of the devices show the flat glow discharge which was also present in figure 3.13. However, only in the BDD substrate device operated in 2300 Torr He (orange) exhibited an abnormal glow voltage increase, due to the complete covering of the cathode surface. The rest of the devices were characterised at much lower pressures, which likely made it possible for the plasma to expand out of the cathode hollow at higher currents, allowing both the cathode surface and copper lid to support the plasma and keep the discharge within the normal glow regime.

3.6.1. Interesting I-V Curve Features

At low frequencies of 10 Hz, in the event that a smooth I-V curve relatively free from instabilities could be recorded, a hysteresis loop between the up and down ramps of the current was recorded, shown clearly in one of the p-Si devices in figure 3.14. Due to the lower pressure operation of three of the devices, the plasma was able to expand out of the cathode hollow and onto the copper lid. Secondary electron emission from the copper could be sustaining the plasma as it shrunk, giving the plasma this asymmetric voltage behaviour.

Another interesting and unexpected feature on the p-Si I-V curves produced in figure 3.14 is the presence of a ohmic, sharply increasing voltage at non-zero current values. This is thought to be due to the presence of the previously described sputtered and melted layer of silicon, which covers

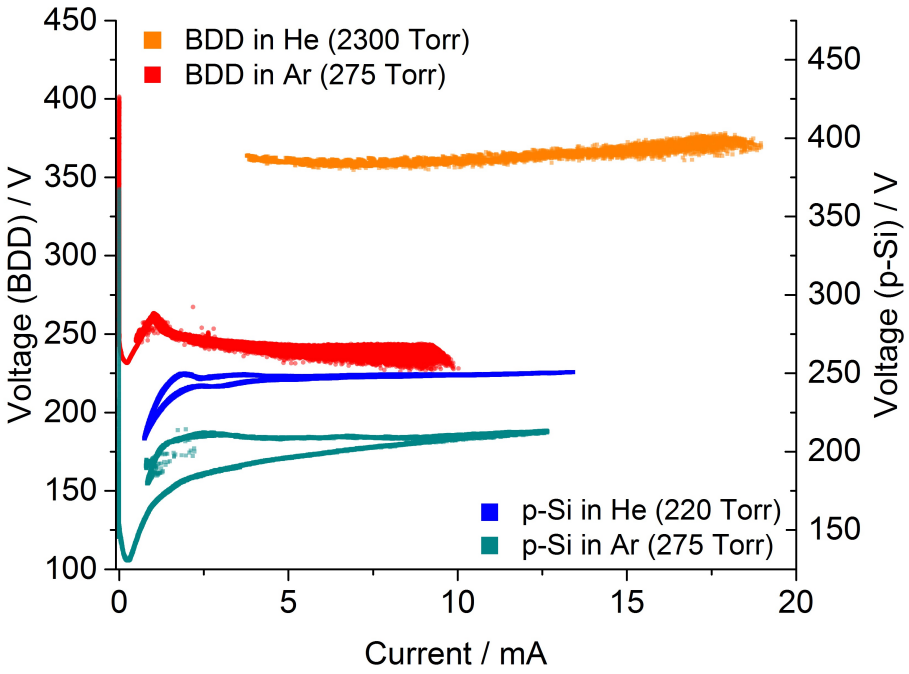

Figure 3.14: Four I-V curves measured using 3 devices with p-Si or BDD cathodes. The plots represent discharges in both Ar and He environments, showing consistency between the relationship of current and voltage.

the cathode and dielectric layers, creating a resistive, alternate electrical pathway between the anode and cathode. Once the voltage had increased to sufficient values, the gas could breakdown fully, forming the normal and abnormal glow discharge characteristics.

4. Afterword

4.1. Conclusion

Microdischarges, or microplasmas, allow generation of highly non-thermal plasma at pressures approaching or exceeding atmospheric pressure. Moving away from ultra-low pressure, high volume plasma production allows glow discharges operate in a highly collisional regime, with many useful consequences. However, high current density and power conditions can result in strong sputtering and damage to the microdischarge electrodes, often causing such microdicharge devices to have lifetimes on the order of hours. Advances in chemical vapour deposition technologies over the last 20 years have allowed polycrystalline diamond films to be investigated for use within microdischarge device fabrication, due to its favourable thermal expansion and thermal conductivity coefficient coupled with the ability to create p-type polycrystalline diamond electrodes through doping.

Over 20 working microdischarge devices based on a hollow cathode electrode-dielectric-electrode sandwich structure were fabricated. A MWCVD deposition process was used to grow an insulating intrinsic diamond layer onto cathode substrates, followed by laser machining of a hollow. The cathodes of these devices were either boron-doped diamond (BDD) wafers or extrinsic silicon wafers, both purchased from external sources. The laser milled cavities measured either 150 µm or 300 µm in diameter. An improved device holder was constructed to include a hollow anode and channel to promote the removal of graphite and other material produced during device operation by convection, as well as an improved system for alignment of the device hollow with the copper lid.

The overall aim of the project was to investigate the differences in the breakdown behaviour and I-V characteristics of BDD cathode and silicon cathode devices and how changes to the cathode, both chemically and morphologically, altered this behaviour. Devices were operated at pressures between 50 and 3000 Torr in a range of gases at currents ranging 0.1 - 20 mA, with stable operation observed in most devices. Breakdown of the devices to the glow discharge was found to be similar between devices of n-type silicon, p-type silicon and BDD, with changes to the cathode morphology and chemical composition deemed an important factor in the determination of the breakdown voltage with changing pressure.

Through SEM imaging, the thickness of the dielectric layer of the tested devices was found to vary from 15 µm to 40 µm between MWCVD growth batches, caused by differences in substrate temperatures. This variance made direct comparison of device breakdown behaviour challenging due to the effect dielectric thickness has on the electric field within the hollow.

During operation in He and Ar gases, silicon and BDD cathodes were found to suffer contrasting changes to their surface composition and chemical composition, altering their breakdown behaviour between subsequent measurements. The surface of the BDD cathode is heavily eroded by operation in Ar and less considerably by He. Bombardment of the cathode by gas ions resulted in the conversion of diamond-like carbon to conducting graphite and the non-uniform extension of the cavity diameter. The formation of conductive graphite onto the surface was found in some cases to also cover the dielectric, allowing current flow between the electrodes without gas breakdown. In many cases, due to limitations in the available area of the cathode able to support plasma, the

eroded cathode caused the glow discharge to be hidden from view, negating any applications of direct radiation emission.

Silicon based devices suffered sputtering and re-deposition of silicon onto the surface, in addition to the potential formation of insulating silicon nitride and silicon oxide surface species. While the external shape of the hollow was maintained by this re-deposition, the porous morphology and insulating properties resulted in increased breakdown voltages at higher pressures compared to preceding breakdown measurements. The rate of damage to silicon cathode devices was also higher than BDD cathode devices, with a porous conducting surface layer forming quicker than the formation of an etched secondary hollow in the BDD cathode cavity. Breakdown behaviour of both silicon and BDD cathode devices were different to behaviour in previous studies, most likely due to changes to the cathode hollow from previous breakdown and I-V characterisation.

The I-V behaviour of p-type silicon and BDD cathode devices was also characterised, showing operation of the devices within the glow discharge regime at pressures of 300 and 2300 Torr, in agreement with literature and previous work. The abnormal glow was not reached when devices were operated at lower pressures (300 Torr) due to spreading of the plasma to the copper lid at high currents, stopping the cathode surface being completely covered. However, the characteristic rise of the sustaining voltage signalling the abnormal glow transition was observed at 2300 Torr, as high pressures restrict the glow discharge to within the cathode hollow where its surface can then be completely covered. An interesting voltage rise during the increasing current ramp for silicon cathode devices was also observed, possibly due to the presence of an alternative, moderately resistive electrical path which operates in tandem with conduction through the discharge gas until the gas is sufficiently ionized.

The breakdown behaviour of 4 MHCD devices was fitted with a modified Paschen's law, using a minimised least squares fit of multiple curves simultaneously, with some constants fitted consistently between the curve fits. It was found that modifications to the cathode surface resulted in increases to A and B, indicating a reduction in the electron mean free path and therefore long path breakdown. However, due to the correlation of all 3 parameters (A, B and γ), it was not possible to differ values of γ between curve fits, which would be a strong indicator of surface modification. Strong correlation between A and γ also resulted in the possibility of generating a large number of A-γ combinations to fit the breakdown data, making conclusions challenging to substantiate.

Diamond cathode based devices have been shown to offer substantial advantages over microdischarge devices with cathodes of metal or silicon, in terms of resistance to ion bombardment, thermal expansion and conductivity. While the electrical properties of BDD cathode devices seem similar to more easily machined silicon cathode devices, increases in device lifetime and the mode of devices failure make diamond cathode based devices a promising candidate for long term, low current microplasma applications, having shown lifetimes of several hours at current densities orders of magnitude higher than those reported in literature.

4.2. Further Work

4.2.1. The Rate of Cathode Morphology Changes

The condition of the cathode cavity surfaces were imaged via SEM only once significant characterisation of its breakdown characteristics and I-V characteristics had been carried out. I-V characterisation involved high current densities which would rapidly modify the morphology of the cathode hollow relative to lower current breakdown studies. Bisection of a series of identical devices operated at equal currents for varying time periods should allow a better understanding of how long it takes for the cathode surface to be significantly modified, either through formation of graphite, shorting circuiting the device or the creation of a porous re-deposited layer.

4.2.2. Chemical Composition of the Porous Cathode Surface

It has been reported in literature that the porous surface which forms in silicon cathode devices to be solely re-deposited Silicon. However, the presence of N_2 and O_2 in the imperfect vacuum system or in the source gases could allow formation of oxide and nitride species not previously seen. EDX analysis of the porous layer would show if insulating layers play an important part in the modification of the breakdown characteristics compared to the re-deposition of less highly doped silicon onto the cavity surface.

4.2.3. Device Lifetimes

Previous work using BDD cathode devices in He has shown device lifetimes of ca. 6 hours before short-circuiting due to graphite build up. The creation of a new device holder containing an hollow anode allowing conductive graphite (and potentially sputtered silicon) to be removed via convection should be expected to increase the lifetime of the devices, but has not been investigated. Studies of the lifetimes of both BDD and silicon cathode devices in He and Ar could identify the potential of low cost, low current microdischarge devices with diamond or silicon electrodes, replacing metal electrode microdischarges.

4.2.4. Changes to the Fabrication Process

Due to varying thickness of the insulating diamond dielectric layer, the fabricated MHCD devices could not be directly compared due to differences in the aspect ratio of the glow discharges which form within the cavity. In order to allow the formation of a dielectric layer to be consistent across a single batch of substrates, only substrates of the same material should be grown together.

4.3. Acknowledgements

I would like to thank Dr. Ben Truscott first and foremost, for his attentive supervision throughout the project. His intelligent and thoughtful input into both practical and theoretical aspects of the project have been invaluable.

I would also like to thank Dr. James Smith for his help in many practical aspects of the project and Professor Paul May, Professor Mike Ashfold and Dr. Neil Fox for their helpful discussions and advice. Thanks also to Dr. Zamir Othman for help in preparing substrates for diamond growth, Alex Croot for his help in operating the SEM and Ingebjørg Narvestad Hungnes for tirelessly seeking out and correcting many an erroneous sentence.

References

[1] J. Achard, A. Tallaire, R. Sussmann, F. Silva and A. Gicquel. *The control of growth parameters in the synthesis of high-quality single crystalline diamond by CVD. J. Cryst. Growth*, **284** 3-4 396–405, 2005. doi:10.1016/j.jcrysgro.2005.07.046.

[2] F. Adler, E. Davliatchine and E. Kindel. *Comprehensive parameter study of a micro-hollow cathode discharge containing xenon. J. Phys. D: Appl. Phys.*, **35** 18 2291, 2002. doi:10.1088/0022-3727/35/18/310.

[3] Alan J. Lichtenberg Michael A. Lieberman. *Principles of Plasma Discharges and Materials Processing*. 2nd edition (Wiley-Interscience, 2005).

[4] M. N. R. Ashfold, P. W. May, C. A. Rego and N. M. Everitt. *Thin film diamond by chemical vapour deposition methods. Chem. Soc. Rev.*, **23** 1 21, 1994. doi:10.1039/cs9942300021.

[5] E. Badareu and I. Popescu. *Researches on the Double Cathode Effect. J. Electron. Control*, **4** 6 503–514, 1958. doi:10.1080/00207215808953873.

[6] K. H. Becker, P. F. Kurunczi and K. H. Schoenbach. *Collisional and radiative processes in high-pressure discharge plasmas. Phys. Plasmas*, **9** 5 2399–2404, 2002. doi:10.1063/1.1449464.

[7] K. H. Becker, K. H. Schoenbach and J. G. Eden. *Microplasmas and applications. J. Phys. D: Appl. Phys.*, **39** 3 R55–R70, 2006. doi:10.1088/0022-3727/39/3/R01.

[8] S. G. Belostotskiy, R. Khandelwal, Q. Wang, V. M. Donnelly, D. J. Economou and N. Sadeghi. *Measurement of electron temperature and density in an argon microdischarge by laser Thomson scattering. Appl. Phys. Lett.*, **92** 22 11–14, 2008. doi:10.1063/1.2939437.

[9] H. Boenig. *Fundamentals of plasma chemistry and technology* (Technomic Pub. Co., 1988).

[10] J. P. Boeuf, L. C. Pitchford and K. H. Schoenbach. *Predicted properties of microhollow cathode discharges in xenon. Appl. Phys. Lett.*, **86** 7 071501, 2005. doi:10.1063/1.1862781.

[11] P. Butler-Smith, D. Axinte, M. Pacella and M. Fay. *Micro/nanometric investigations of the effects of laser ablation in the generation of micro-tools from solid CVD diamond structures. J. Mater. Process. Technol.*, **213** 2 194–200, 2013. doi:10.1016/j.jmatprotec.2012.08.010.

[12] T. Callegari, X. Aubert, A. Rousseau, J. P. Boeuf and L. C. Pitchford. *Microhollow cathode sustained discharges: comparative studies in micro- and equivalent macro-cell geometries. Eur. Phys. J. D*, **60** 3 581–587, 2010. doi:10.1140/epjd/e2010-00229-x.

[13] B. Chapman. *Glow Discharge Processes: Sputtering and Plasma Etching* (Wiley, 1980).

[14] J. Chen, S.-J. Park, A. Member, Z. Fan, J. G. Eden and C. Liu. *Development and Characterization of Micromachined Hollow Cathode Plasma Display Devices. J. Microelecromech. Syst.*, **11** 5 536–543, 2002. doi:10.1109/JMEMS.2002.802907.

[15] G. Chryssolouris. *Laser machining: Theory and Practice*. Mechanical engineering series (Springer-Verlag, 1991).

[16] J. Cobine. *Gaseous Conductors: Theory and Engineering Applications* (Dover Publications, 1958).

[17] D. A. Frank-Kamenetskii. *Plasma - The Forth State of Matter* (The Macmillan Press, Ltd., London, 1972).

[18] A. El-Habachi and K. H. Schoenbach. *Generation of intense excimer radiation from high-pressure hollow cathode discharges. Appl. Phys. Lett.*, **73** 7 885, 1998. doi:10.1063/1.122027.

[19] J. Feichtinger, A. Schulz, M. Walker and U. Schumacher. *Sterilisation with low-pressure microwave plasmas. Surf. Coatings Technol.*, **174-175** 564–569, 2003. doi:10.1016/S0257-8972(03)00404-3.

[20] H. Feng, H. Shoujie, Z. Xiaofei, G. Bingang, O. Jiting, F. He, S. He, X. Zhao, B. Guo and J. Ouyang. *Study of the Discharge Mode in Micro-Hollow Cathode. Plasma Sci. Technol.*, **14** 12 1079, 2012. doi:10.1088/1009-0630/14/12/08.

[21] R. Foest, M. Schmidt and K. Becker. *Microplasmas, an emerging field of low-temperature plasma science and technology. Int. J. Mass Spectrom.*, **248** 3 87–102, 2006. doi:10.1016/j.ijms.2005.11.010.

[22] J. Frame and J. Eden. *Planar microdischarge arrays. Electron. Lett.*, **34** 15 1529–1531, 1998. doi:10.1049/el:19981018.

[23] J. W. Frame, D. J. Wheeler, T. A. DeTemple and J. G. Eden. *Microdischarge devices fabricated in silicon. Appl. Phys. Lett.*, **71** 9 1165, 1997. doi:10.1063/1.119614.

[24] V. I. Gibalov and G. J. Pietsch. *The development of dielectric barrier discharges in gas gaps and on surfaces. J. Phys. D: Appl. Phys.*, **33** 20 2618, 2000.

[25] P. Gill and C. E. Webb. *Electron energy distributions in the negative glow and their relevance to hollow cathode lasers. J. Phys. D: Appl. Phys.*, **10** 3 299–301, 1977. doi:10.1088/0022-3727/10/3/010.

[26] M. P. Gomes, B. N. Sismanoglu and J. Amorim. *Characterization of microhollow cathode discharges. Brazilian J. Phys.*, **39** 1 25–30, 2009. doi:10.1590/S0103-97332009000100004.

[27] X.-L. Hao, M.-H. Zhou, Y. Zhang and L.-C. Lei. *Enhanced degradation of organic pollutant 4-chlorophenol in water by non-thermal plasma process with TiO2. Plasma Chem. Plasma Process.*, **26** 5 455–468, 2006. doi:10.1007/s11090-006-9028-0.

[28] P. M. Harrison, M. Henry and M. Brownell. *Laser processing of polycrystalline diamond, tungsten carbide, and a related composite material. J. Laser Appl.*, **18** 2 117–126, 2006. doi:10.2351/1.2164472.

[29] A. Hatta, H. Nakatsuma, K. Yanai and T. Nishikawa. *Cold Cathode of p-Type Semiconducting Diamond Films for Gas Discharge. Plasma Process. Polym.*, **4** S1 S942–S945, 2007. doi:10.1002/ppap.200732304.

[30] W. Haynes. *CRC Handbook of Chemistry and Physics, 96th Edition.* CRC Handbook of Chemistry and Physics (Taylor & Francis, 2015).

[31] A. Heylen. *Sparking formulae for very high-voltage Paschen characteristics of gases. IEEE Electr. Insul. Mag.*, **22** 3 25–35, 2006. doi:10.1109/MEI.2006.1639027.

[32] F. J. Himpsel, J. A. Knapp, J. A. VanVechten and D. E. Eastman. *Quantum photoyield of diamond(111)¯a stable negative-affinity emitter. Phys. Rev. B*, **20** 624–627, 1979. doi:10.1103/PhysRevB.20.624.

[33] Y. Hoshi and H. Yoshida. *Examination of laser-triggered discharge using a virtual gas model and the similarity of its Paschen curve with those of inert gases. J. Appl. Phys.*, **106** 6 066103, 2009. doi:10.1063/1.3223536.

[34] A. M. Howatson. *An Introduction to Gas Discharges.* 2nd edition (Pergamon, 1965).

[35] D. D. Hsu and D. B. Graves. *Microhollow cathode discharge stability with flow and reaction. J. Phys. D: Appl. Phys.*, **36** 23 2898, 2003. doi:10.1088/0022-3727/36/23/006.

[36] S. Kanazawa, M. Kogoma, T. Moriwaki and S. Okazaki. *Stable glow plasma at atmospheric pressure. J. Phys D Appl. Phys.*, **21** 5 838–840, 1988. doi:10.1088/0022-3727/21/5/028.

[37] A. Kershaw. *High Pressure Microplasma in Diamond and Silicon Substrates* ((Master's thesis). University of Bristol, 2015).

[38] G. J. Kim, F. Iza and J. K. Lee. *Electron and ion kinetics in a micro hollow cathode discharge. J. Phys. D. Appl. Phys.*, **39** 20 4386, 2006. doi:10.1088/0022-3727/39/20/014.

[39] H. H. Kim, G. Prieto, K. Takashima, S. Katsura and A. Mizuno. *Performance evaluation of discharge plasma process for gaseous pollutant removal. J. Electrostat.*, **55** 1 25–41, 2002. doi:10.1016/S0304-3886(01)00182-6.

[40] A. Koutsospyros, S.-M. Yin, C. Christodoulatos and K. Becker. *Destruction of hydrocarbons in non-thermal, ambient-pressure, capillary discharge plasmas. Int. J. Mass Spectrom.*, **233** 1-3 305–315, 2004. doi:10.1016/j.ijms.2003.12.033.

[41] A. D. Koutsospyros, S.-M. Yin, C. Christodoulatos and K. Becker. *Plasmochemical degradation of volatile organic compounds (VOC) in a capillary discharge plasma Reactor. IEEE Trans. Plasma Sci.*, **33** 1 42–49, 2005. doi:10.1109/TPS.2004.841925.

[42] M. K. Kulsreshath, L. Schwaederle, L. J. Overzet, P. Lefaucheux, J. Ladroue, T. Tillocher, O. Aubry, M. Woytasik, G. Schelcher and R. Dussart. *Study of dc micro-discharge arrays made in silicon using CMOS compatible technology. J. Phys. D. Appl. Phys.*, **45** 28 285202, 2012. doi:10.1088/0022-3727/45/28/285202.

[43] P. Kurunczi, J. Lopez, H. Shah and K. Becker. *Excimer formation in high-pressure microhollow cathode discharge plasmas in helium initiated by low-energy electron collisions. Int. J. Mass Spectrom.*, **205** 1-3 277–283, 2001. doi:10.1016/S1387-3806(00)00377-8.

[44] P. Kurunczi, K. Martus and K. Becker. *Neon excimer emission from pulsed high-pressure microhollow cathode discharge plasmas. Int. J. Mass Spectrom.*, **223-224** 37–43, 2003. doi:10.1016/S1387-3806(02)00778-9.

[45] P. Kurunczi, H. Shah and K. Becker. *Hydrogen Lyman-alpha and Lyman-beta emissions from high-pressure microhollow cathode discharges in Ne-H 2 mixtures. J. Phys. B: At. Mol. Opt. Phys.*, **32** 22 L651–L658, 1999. doi:10.1088/0953-4075/32/22/103.

[46] M. J. Kushner. *Modeling of microdischarge devices: Pyramidal structures. J. Appl. Phys.*, **95** 3 846–859, 2004. doi:10.1063/1.1636251.

[47] M. J. Kushner. *Modelling of microdischarge devices: plasma and gas dynamics. J. Phys. D. Appl. Phys.*, **38** 11 1633–1643, 2005. doi:10.1088/0022-3727/38/11/001.

[48] M. Laroussi. *Low Temperature Plasma-Based Sterilization: Overview and State-of-the-Art. Plasma Process. Polym.*, **2** 5 391–400, 2005. doi:10.1002/ppap.200400078.

[49] M. Laroussi, I. Alexeff, J. Richardson and F. Dyer. *The resistive barrier discharge. IEEE Trans. Plasma Sci.*, **30** 1 158–159, 2002. doi:10.1109/TPS.2002.1003972.

[50] V. A. Lisovsky and S. D. Yakovin. *Scaling law for a low-pressure gas breakdown in a homogeneous DC electric field. J. Exp. Theor. Phys. Lett.*, **72** 2 34–37, 2000. doi:10.1134/1.1312005.

[51] X. Lu, S. Wu, J. Gou and Y. Pan. *An atmospheric-pressure, high-aspect-ratio, cold microplasma. Scientific Reports*, **4** 7488, 2014. doi:10.1038/srep07488.

[52] K. Makasheva, E. Muñoz Serrano, G. Hagelaar, J.-P. Boeuf and L. C. Pitchford. *A better understanding of microcathode sustained discharges. Plasma Phys. Control. Fusion*, **49** 12B B233–B238, 2007. doi:10.1088/0741-3335/49/12B/S21.

[53] J. Meichsner. *Nonthermal plasma chemistry and physics* (CRC Press, 2013).

[54] M. Miclea (Editor). *HAKONE 8: International Symposium on High Pressure, Low Temperature Plasma Chemistry*, volume 1 (2002).

[55] S. Mitea, M. Zeleznik, M. D. Bowden, P. W. May, N. A. Fox, J. N. Hart, C. Fowler, R. Stevens and N. S. Braithwaite. *Generation of microdischarges in diamond substrates. Plasma Sources Sci. Technol.*, **21** 2 22001, 2012. doi:10.1088/0963-0252/21/2/022001.

[56] B. Mitra, B. Levey and Y. B. Gianchandani. *Hybrid Arc / Glow Microdischarges at Atmospheric Pressure and Their Use in Portable Systems for Liquid and Gas Sensing. IEEE Trans. Plasma Sci.*, **36** 4 1913–1924, 2008.

[57] A. Mizuno. *Industrial applications of atmospheric non-thermal plasma in environmental remediation. Plasma Phys. Control. Fusion*, **49** 5A A1, 2007. doi:10.1088/0741-3335/49/5A/S01.

[58] M. Moselhy, I. Petzenhauser, K. Frank and K. H. Schoenbach. *Excimer emission from microhollow cathode argon discharges. J. Phys. D. Appl. Phys.*, **36** 23 2922, 2003. doi:10.1088/0022-3727/36/23/009.

[59] M. Moselhy and K. H. Schoenbach. *Excimer emission from cathode boundary layer discharges. J. Appl. Phys.*, **95** 4 1642–1649, 2004. doi:10.1063/1.1640789.

[60] E. Nasser. *Fundamentals of gaseous ionization and plasma electronics.* Wiley Series in Plasma Physics (John Wiley & Sons Canada, Limited, 1971).

[61] M. T. Ngo, K. H. Schoenbach, G. a. Gerdin and J. H. Lee. *Temporal development of hollow cathode discharges. IEEE Trans. Plasma Sci.*, **18** 3 669–676, 1990. doi:10.1109/27.55942.

[62] H. I. Park, T. I. Lee, K. W. Park, H. K. Baik, S.-J. Lee and K. M. Song. *Formation of large-volume, high-pressure plasmas in microhollow cathode discharges. Appl. Phys. Lett.*, **82** 19 3191, 2003. doi:10.1063/1.1573359.

[63] S.-J. Park and J. G. Eden. *1330 micron diameter microdischarge devices: Atomic ion and molecular emission at above atmospheric pressures. Appl. Phys. Lett.*, **81** 22 4127, 2002. doi:10.1063/1.1520707.

[64] S.-J. Park, C. Wagner and J. Eden. *Performance of microdischarge devices and arrays with screen electrodes. IEEE Photonics Technol. Lett.*, **13** 1 61–63, 2001. doi:10.1109/68.903221.

[65] F. Paschen. *Ueber die zum Funkenübergang in Luft, Wasserstoff und Kohlensäure bei verschiedenen Drucken erforderliche Potentialdifferenz. Annalen der Physik*, **273** 69–96, 1889. doi:10.1002/andp.18892730505.

[66] F. Penning. *Electrical discharges in gases* (Macmillian, 1957).

[67] F. M. Penning. *Electrical discharges in gases*. Miscellaneous series (Macmillian, 1957).

[68] I. Petzenhauser, L. D. Biborosch, U. Ernst, K. Frank and K. H. Schoenbach. *Comparison between the ultraviolet emission from pulsed microhollow cathode discharges in xenon and argon. Appl. Phys. Lett.*, **83** 21 4297–4299, 2003. doi:Doi 10.1063/1.1626020.

[69] D. Q. Posin. *The Townsend Coefficients and Spark Discharge. Phys. Rev.*, **50** 7 650–658, 1936. doi:10.1103/PhysRev.50.650.

[70] O. B. Postel and M. A. Cappelli. *Vacuum emission and breakdown characteristics of a planar HeXe microdischarge. Appl. Phys. Lett.*, **76** 5 544, 2000. doi:10.1063/1.125813.

[71] H. Qiu, K. Martus, W. Y. Lee and K. Becker. *Hydrogen generation in a microhollow cathode discharge in high-pressure ammonia-argon gas mixtures. Int. J. Mass Spectrom.*, **233** 1-3 19–24, 2004. doi:10.1016/j.ijms.2003.08.017.

[72] R. J. Goldston and P. H. Rutherford. *Introduction to Plasma Physics*. In *Introduction to Plasma Physics*, chapter 1 (Taylor & Francis, 1995).

[73] Y. P. Raizer, J. E. Allen and V. Kisin. *Gas discharge physics* (Springer, 1991).

[74] Richard D. Hazeltine and Franois L. Waelbroeck. *The Framework of Plasma Physics*. Frontiers in Physics (Perseus Books, Reading, MA, 1998).

[75] R. M. Sankaran and K. P. Giapis. *Hollow cathode sustained plasma microjets: Characterization and application to diamond deposition. J. Appl. Phys.*, **92** 5 2406–2411, 2002. doi:10.1063/1.1497719.

[76] A. Savitzky and M. J. E. Golay. *Smoothing and differentiation of data by simplified least squares procedures. Anal. Chem.*, **36** 1627, 1964.

[77] G. Schaefer and K. Schoenbach. *Basic mechanisms contributing to the hollow cathode effect*. In M. Gundersen and G. Schaefer (Editors), *Physics and Applications of Pseudosparks*, volume 219 of *NATO ASI Series*, pp. 55–76 (Springer US, 1990). doi:10.1007/978-1-4615-3786-1_3.

[78] K. H. Schoenbach and K. Becker. *20 Years of Microplasma Research: a Status Report. Eur. Phys. J. D*, **70** 2 29, 2016. doi:10.1140/epjd/e2015-60618-1.

[79] K. H. Schoenbach, A. El-Habachi, M. M. Moselhy, W. Shi and R. H. Stark. *Microhollow cathode discharge excimer lamps. Phys. Plasmas*, **7** 2000 2186, 2000. doi:10.1063/1.874039.

[80] K. H. Schoenbach, A. El-Habachi, W. Shi and M. Ciocca. *High-pressure hollow cathode discharges. Plasma Sources Sci. Technol.*, **6** 4 468–477, 1997. doi:10.1088/0963-0252/6/4/003.

[81] K. H. Schoenbach, M. Moselhy and W. Shi. *Self-organization in cathode boundary layer microdischarges. Plasma Sources Sci. Technol.*, **13** 1 177–185, 2004. doi:10.1088/0963-0252/13/1/023.

[82] K. H. Schoenbach, M. Moselhy, W. Shi and R. Bentley. *Microhollow cathode discharges. J. Vac. Sci. Technol. A*, **21** 4 1260–1265, 2003. doi:http://dx.doi.org/10.1116/1.1565154.

[83] K. H. Schoenbach, R. Verhappen, T. Tessnow, F. E. Peterkin and W. W. Byszewski. *Microhollow cathode discharges. Appl. Phys. Lett.*, **68** 1 13–15, 1995. doi:10.1063/1.116739.

[84] K. H. Schoenbach and W. Zhu. *High-Pressure Microdischarges: Sources of Ultraviolet Radiation. IEEE J. Quantum Electron.*, **48** 6 768–782, 2012. doi:10.1109/JQE.2012.2185686.

[85] R. H. Stark and K. H. Schoenbach. *Direct current high-pressure glow discharges. J. Appl. Phys.*, **85** 4 2075, 1999. doi:10.1063/1.369505.

[86] R. H. Stark and K. H. Schoenbach. *Electron heating in atmospheric pressure glow discharges. J. Appl. Phys.*, **89** 7 3568, 2001. doi:10.1063/1.1351546.

[87] K. D. Stephan, S. Ghimire, R. K. Smith, L. Komala-Noor and N. Massey. *Transverse Stabilization of Atmospheric-Pressure DC Glow Plasma in Air With Resistive Barrier. IEEE Trans. Plasma Sci.*, **39** 10 1919–1926, 2011. doi:10.1109/TPS.2011.2163735.

[88] T. J. M. Boyd and J. J. Sanderson. *The Physics of Plasmas* (Cambridge University Press, Cambridge, 2003).

[89] K. Tachibana. *Current status of microplasma research. IEEJ Trans. Electr. Electron. Eng.*, **1** 2 145–155, 2006. doi:10.1002/tee.20031.

[90] B. S. Truscott, C. Turner and P. W. May. *High-pressure dc glow discharges in hollow diamond cathodes. Plasma Sources Sci. Technol.*, **25** 2 025005, 2016. doi:10.1088/0963-0252/25/2/025005.

[91] C. Turner. *Investigating High Pressure Microplasmas in Diamond Substrates* ((Master's thesis). University of Bristol, 2013).

[92] P. von Allmen, D. J. Sadler, C. Jensen, N. P. Ostrom, S. T. McCain, B. A. Vojak and J. G. Eden. *Linear, segmented microdischarge array with an active length of 1 cm: cw and pulsed operation in the rare gases and evidence of gain on the 460.30 nm transition of xe+. Appl. Phys. Lett.*, **82** 25 4447, 2003. doi:10.1063/1.1585137.

[93] A. von Engel. *Ionised Gases* (Oxford : Clarendon Press, 1965).

[94] C. J. Wagner, S.-J. Park and J. G. Eden. *Excitation of a microdischarge with a reverse-biased pn junction. Appl. Phys. Lett.*, **78** 6 709, 2001. doi:10.1063/1.1345838.

[95] J. L. Walsh, F. Iza and M. G. Kong. *Characterisation of a 3 nanosecond pulsed atmospheric pressure argon microplasma. Eur. Phys. J. D*, **60** 3 523–530, 2010. doi:10.1140/epjd/e2010-00238-9.

[96] A. D. White. *New Hollow Cathode Glow Discharge. J. Appl. Phys.*, **30** 5 711, 1959. doi:10.1063/1.1735220.

[97] Z. Yu, K. Hoshimiya, J. D. Williams, S. F. Polvinen and G. J. Collins. *Radio-frequency-driven near atmospheric pressure microplasma in a hollow slot electrode configuration. Appl. Phys. Lett.*, **83** 5 854, 2003. doi:10.1063/1.1564640.

A. Appendices

A.1. Calculating the Milled Cavity Location

The substrate was held in place inside the high pressure chamber using the clip shown in figure 2.3. The relative locations of the cavities to be milled are labelled 6, 7, 8, 9 and substrate corners 1, 2, 3, 4, shown in figure A.1. In order to determine the location of the 4 cavities within the corners of the substrate, the absolute positions of corners 1, 2 and 3 were measured by observation using the absolute measuring system of the macro-machining laser system.

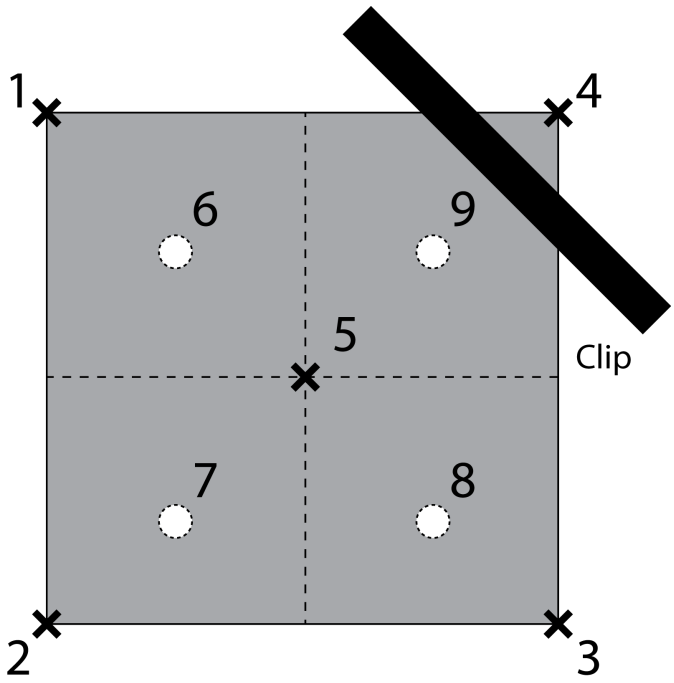

Figure A.1: Diagram showing the labelled corners of the substrate and the relative positions of the cavities to be calculated from the positions of 3 of the corners.

Assuming reasonable uniformity in the dimensions of the substrate, the absolute position of the centre was calculated using equations A1.1, followed by calculation of the absolute position of the 4th corner which is hidden by the holding clip, via equation A1.2.

$$\boldsymbol{r_5} = \frac{1}{2}(\boldsymbol{r_1} + \boldsymbol{r_3}) \tag{A1.1}$$

$$\boldsymbol{r_4} = 2(\boldsymbol{r_5} - \boldsymbol{r_2}) \tag{A1.2}$$

where $\boldsymbol{r_i}$ is the (x,y) position of corner i.

Once $\boldsymbol{r_4}$ was known, the positions of all 4 cavities could be calculated using the midpoint of the corresponding corner and the substrate centre. The calculation of the absolute position of cavity 1 ($\boldsymbol{r_6}$) is shown in equation A1.3.

$$\boldsymbol{r_6} = \frac{1}{2}(\boldsymbol{r_1} + \boldsymbol{r_5}) \tag{A1.3}$$